frontiers in NEUROLOGY

ORIGINAL RESEARCH ARTICLE
published: 11 March 2014
doi: 10.3389/fneur.2014.00026

Biochemical distribution of tau protein in synaptosomal fraction of transgenic mice expressing human P301L tau

Naruhiko Sahara[1,2]*, Miyuki Murayama[2], Makoto Higuchi[1], Tetsuya Suhara[1] and Akihiko Takashima[2,3]

[1] Molecular Imaging Center, National Institute of Radiological Sciences, Chiba, Japan
[2] Laboratory for Alzheimer's Disease, RIKEN Brain Science Institute, Wako, Japan
[3] Department of Aging Neurobiology, National Center for Geriatrics and Gerontology, Obu, Japan

Edited by:
Ritchie Williamson, University of Dundee, UK

Reviewed by:
Jurgen Gotz, The University of Sydney, Australia
Masashi Kitazawa, University of California, Merced, USA

***Correspondence:**
Naruhiko Sahara, Molecular Imaging Center, National Institute of Radiological Sciences, 4-9-1 Anagawa, Inage-ku, Chiba-shi, Chiba 263-8555, Japan
e-mail: nsahara@nirs.go.jp

Alzheimer's disease is a progressive dementia that is characterized by a loss of recent memory. Evidence has accumulated to support the hypothesis that synapses are critical storage sites for memory. However, it is still uncertain whether tau protein is involved in associative memory storage and whether tau is distributed in mature brain synapses. To address this question, we examined the synaptosomal distribution of tau protein in both JNPL3 transgenic mice expressing human P301L tau and non-transgenic littermates. The JNPL3 mouse line is known as one of the mouse models of human tauopathy that develop motor and behavioral deficits with intracellular tau aggregates in the spinal cord and brainstem. The phenotype of disease progression is highly dependent on strain background. In this study, we confirmed that male JNPL3 transgenic mice with C57BL/6J strain background showed neither any sign of motor deficits nor accumulation of hyperphosphorylated tau in the sarkosyl-insoluble fraction until 18 months of age. Subcellular fractionation analysis showed that both mouse tau and human P301L tau were present in the synaptosomal fraction. Those tau proteins were less-phosphorylated than tau in the cytosolic fraction. Human P301L tau was preferentially distributed in the synaptosomal fraction while mouse endogenous tau was more distributed in the cytosolic fraction. Interestingly, a human-specific tau band with phosphorylation at Ser199 and Ser396 was observed in the synaptosomal fraction of JNPL3 mice. This tau was not identical to either tau species in cytosolic fraction or a prominent hyperphosphorylated 64 kDa tau species that was altered to tau pathology. These results suggest that exogenous human P301L tau induces synaptosomal distribution of tau protein with a certain phosphorylation. Regulating the synaptosomal tau level might be a potential target for a therapeutic intervention directed at preventing neurodegeneration.

Keywords: P301L tau, transgenic mice, subcellular fractions, synaptosomal fraction, tau phosphorylation

INTRODUCTION

Neurofibrillary tangles (NFTs) and neuronal loss are commonly observed in neurological disorders, including Alzheimer's disease (AD) and other tauopathies (1–3). Brain regions showing dysfunction overlap those displaying NFTs and neuronal loss (4), suggesting that mechanisms of NFT formation and neuronal loss may underlie neuronal dysfunction of affected brain areas. In frontotemporal dementia with Parkinsonism linked to tau on chromosome 17 (FTDP-17-*tau*), tau gene mutations induce NFT formation and neuronal loss (5–8), suggesting that dysregulation of tau may be a cause of NFT formation and neuronal death. This notion is supported by some reports showing that overexpression of FTDP-17-*tau* mutant tau induces NFT formation, neuronal loss, and behavioral abnormalities. In the mouse model rTg4510 overexpressing P301L mutant tau under the regulation of tetracycline, inhibition of mutant tau overexpression in the disease state blocked neuronal death and reversed memory impairment but still induced NFT formation (9), suggesting that NFTs themselves are not toxic, but the mechanism of neuronal death and memory impairment may underlie the process of NFT formation. Although the initial molecular event of tau pathogenesis remains unclear, the hyperphosphorylation of tau is strongly correlated with the severity of the pathology (10). The existence of hyperphosphorylated tau oligomers in human AD brain and transgenic mouse brains supports the idea of neurotoxic tau species (11–15).

Recently, several groups reported the mislocalization of hyperphosphorylated tau into dendritic spines (16–20). Interacting with Fyn kinase, tau contributes to NMDA stabilization (17, 21). Although a novel function of tau in post-synaptic regions was observed, evidence of hyperphosphorylated tau in dendritic spines still requires conclusive confirmation. On the other hand, it is well known that tau is involved in axonal transport stabilization and promotion of microtubule polymerization, and it participates in the transport of vesicles and organelles from axons to synaptic terminals (22). It was also reported that tau overexpression affects axonal transport by obstructing kinesin movement on microtubules (23–26). Since axon was labeled with Tau1 antibody, which recognizes non-phosphorylated tau at Ser199 (27), axonal

tau seems to be de-phosphorylated. Therefore, it is important to clarify the status of tau phosphorylation in synaptic regions. In this study, we investigated the biochemical properties of synaptosomal tau extracted from transgenic mice expressing human P301L mutant tau.

MATERIALS AND METHODS

JNPL3 MICE AND LITTERMATES

Male hemizygous JNPL3 mice were obtained from Taconic Labs (Germantown, NY, USA) at 8 weeks of age. JNPL3 mice express 4R0N isoform of human P301L mutant tau and are characterized as developing NFT, as well as sarkosyl-insoluble tau in an age-dependent manner (28, 29). Transgenic (Tg) mice and non-Tg littermates were bred by mating hemizygous JNPL3 mice with C57BL/6J Jcl (Clea, Tokyo, Japan). The mice were genotyped for the tau transgene by PCR between exons 9 and 13 of human tau cDNA. They were housed under controlled conditions with a 12-h day/night cycle. The age range of both male JNPL3 ($n = 8$) and male non-Tg mice ($n = 5$) was 15.7–18.5 months. Procedures involving animals and their care were approved by the Animal Care and Use Committee of RIKEN.

TISSUE EXTRACTION AND SUBCELLULAR FRACTIONATION

Mice were euthanized by cervical dislocation to preserve the brain metabolic environment and prevent artifacts that could alter tau biochemical profiles. Brains were quick-frozen on dry ice and stored at −80°C. For sarkosyl extraction, the cerebral cortex containing the hippocampus of the left hemibrain was subsequently homogenized in five volumes of Tris–buffer saline (TBS) containing protease and phosphatase inhibitors [25 mM Tris/HCl, pH 7.4, 150 mM NaCl, 1 mM EDTA, 1 mM EGTA, 5 mM sodium pyrophosphate, 30 mM β-glycerophosphate, 30 mM sodium fluoride, and 1 mM phenylmethylsulfonyl fluoride (PMSF)]. The homogenates were centrifuged at 27,000 × *g* for 20 min at 4°C to obtain the supernatant and pellet fractions. Pellets were re-homogenized in five volumes of high salt/sucrose buffer (0.8 M NaCl, 10% sucrose, 10 mM Tris/HCl, pH 7.4, 1 mM EGTA, 1 mM PMSF) and centrifuged as above. The supernatants were collected and incubated with sarkosyl (Sigma, St. Louis, MO, USA; 1% final concentration) for 1 h at 37°C, followed by centrifugation at 150,000 × *g* for 1 h at 4°C to obtain salt and sarkosyl-soluble and sarkosyl-insoluble pellets. The pellets were re-suspended in TE buffer (10 mM Tris/HCl, pH 8.0, 1 mM EDTA) to a volume equivalent to wet weight of the original tissue. For subcellular fractionation, fractions were prepared as previously described (30). Briefly, the cerebral cortex containing the hippocampus of the right hemibrain was Dounce-homogenized with 15 strokes in 10 volumes of homogenization buffer [25 mM Tris/HCl, pH 7.4, 9% sucrose, 2 mM EDTA, 5 mM dithiothreitol, 5 mM 4-(2-aminoethyl)-benzenesulfonyl fluoride hydrochloride (AEBSF), 5 ng/ml Antipain, 2 ng/ml aprotinin, 5 ng/ml leupeptin, 5 ng/ml pepstatin A, 1 μM okadaic acid, 1 mM NaF, 1 mM Na_3VO_4]. Nuclei (P1) were removed by 5 min centrifugation at 1,000 × *g*. The supernatant was subjected to 12,500 × *g* centrifugation for 15 min to yield the crude synaptosomal fraction (P2). The supernatant was centrifuged for 1 h at 176,000 × *g*, resulting in cytosol (S3) and light membrane and Golgi (P3) fractions. Synaptosomal fraction P2 was lysed hypo-osmotically and spun for 20 min at 25,000 × *g* to obtain the synaptosomal membrane fraction LP1. The supernatant was centrifuged for 2 h at 176,000 × *g*, resulting in a synaptic vesicle-enriched fraction (LP2) and a supernatant (LS2).

ANTIBODIES

E1 (31), a polyclonal antibody specific to human tau (aa 19-33, unphosphorylated), was prepared in our laboratory. MS06, a polyclonal antibody specific to mouse tau, was raised against mouse tau polypeptide corresponding to amino acid residue 118–131 (SKDRTGNDEKKAKG). Tau5, pS199, pT231, and pS396 were purchased from Biosource International (Camarillo, CA, USA). Tau1 was from Chemicon (Temecula, CA, USA). Monoclonal antibodies to β-actin and β-tubulin were purchased from Sigma. Monoclonal antibodies to GAP-43, PSD-95, and synaptotagmin were purchased from BD Transduction Laboratories (San Jose, CA, USA). For western blotting, antibodies were used at the following dilutions in blocking solution: E1, 1:5,000; MS06, 1:2,000; Tau1, 1:5,000; Tau5, 1:2,000; pS199, 1:5,000; pT231, 1:2,000; pS396, 1:2,000; β-actin, 1:5,000; β-tubulin, 1:5,000; GAP-43, 1:2,000; PSD-95, 1:2,000; synaptotagmin, 1:2,000.

WESTERN BLOTTING

Fractionated tissue extracts were dissolved in sample buffer containing β-mercaptoethanol (0.01%). The samples were separated by gel electrophoresis on 10 or 5–20% gradient SDS-PAGE gels (Wako Pure Chemical Industries, Osaka, Japan), and transferred to nitrocellulose membranes (Schleicher & Schuell BioScience, Dassel, Germany). To estimate protein molecular weights, molecular size markers (Precision Plus Protein™ Standards, Bio-Rad Laboratories, Hercules, CA, USA; MagicMarker™ XP Western Protein Standard, Life Technologies, Carlsbad, CA, USA) were loaded on each gel. After blocking with a blocking solution containing 5% non-fat milk, 0.1% goat serum, and 0.1% Tween-20 in PBS, the membranes were incubated with various antibodies, washed to remove excess antibodies, and then incubated with peroxidase-conjugated, goat anti-rabbit antibodies (1:5000, Jackson ImmunoResearch, West Grove, PA, USA) or anti-mouse IgG (1:5000, Jackson ImmunoResearch). Bound antibodies were detected using an enhanced chemiluminescence system, SuperSignal West Pico (Pierce Biotechnology, Rockford, IL, USA). Quantitation and visual analysis of immunoreactivity were performed with a computer-linked LAS-3000 Bio-Imaging Analyzer System (Fujifilm, Tokyo, Japan) using the software program Image Gauge 3.0 (Fujifilm).

STATISTICAL ANALYSIS

Statistical analyses were conducted using PRISM4 (GraphPad Software Inc., La Jolla, CA, USA). Data were analyzed using the Friedman test or two-way ANOVA, unless otherwise noted.

RESULTS

EXAMINATION OF SARKOSYL-INSOLUBLE TAU IN MALE JNPL3 MICE

Hemizygous JNPL3 mice were reported to develop motor and behavioral deficits, initially presenting with hind-limb dysfunction starting at 6.5 months (28). These phenotypes were shown with a mixed C57BL/DBA2/SW strain background and mostly in female

mice. Biochemically, subcortical regions contained more sarkosyl-insoluble tau than cortico-limbic regions, and male mice had less sarkosyl-insoluble tau than age-matched female mice (29). Moreover, a previous study showed that JNPL3 mice with C57BL/6J strain background significantly slowed the progression of tau pathology (32). In agreement with these reports, male hemizygous JNPL3 mice on an in-bred C57BL/6J strain at 15–18 months of age did not show any sign of motor deficits. To confirm whether male JNPL3 mice developed pathological tau aggregates in their brains, a sarkosyl-insoluble fraction was prepared using the sarkosyl extraction protocol as previously described (15, 29). Human and mouse tau proteins were detected in the TBS-soluble fraction using anti-human tau-specific antibody E1, anti-mouse tau-specific antibody MS06, and Tau5 antibody recognizing both tau (**Figure 1A**). We observed variable degrees of human tau protein among individual JNPL3 mice when normalized with GAPDH level (**Figure 1A**). In sarkosyl-insoluble fractions from male JNPL3 brains, the hyperphosphorylated tau migrating at 64 kDa was not found, although variable levels of 50 kDa tau bands were detected in this fraction (**Figure 1B**). The hyperphosphorylated 64 kDa tau was a marker of tau pathology in symptomatic JNPL3 and rTg4510 mice expressing the 4R0N isoform of human P301L mutant tau (15, 29). Because of undetectable levels of 64 kDa tau in male JNPL3 cerebral cortices (**Figure 1B**), these male JNPL3 cerebral cortices were considered to likely contain very few pathological tau inclusions.

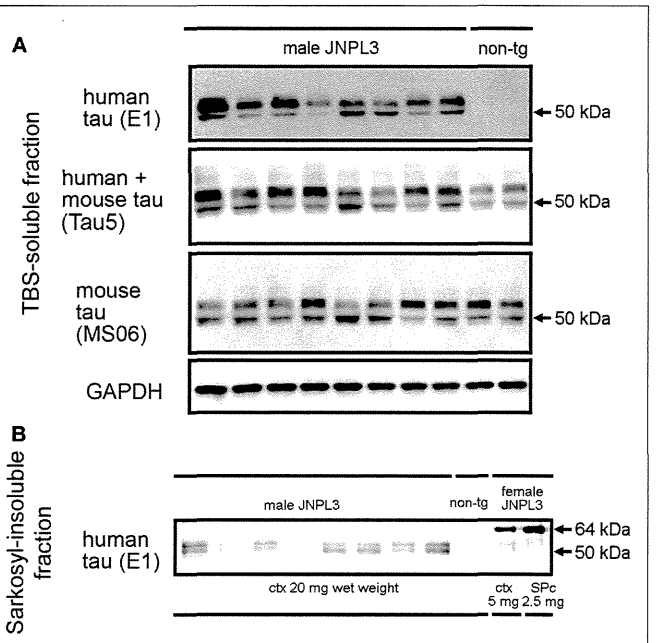

FIGURE 1 | Soluble and sarkosyl-insoluble tau in JNPL3 male mice. **(A)** Western blots of TBS-soluble tau in mouse cerebral cortices. Equal volumes of TBS-soluble fraction derived from 0.2 mg wet weight of brain from eight male JNPL3 and two male non-tg mice were separated by SDS-PAGE, blotted, and then probed with E1, Tau5, MS06, and GAPDH antibodies. **(B)** Western blot of sarkosyl-insoluble fractions in mouse cerebral cortices. Samples derived from 20 mg wet weight from male JNPL3 and non-tg mice, 5 mg wet weight from female JNPL3 cortex (ctx), and 2.5 mg wet weight from female JNPL3 spinal cord (SPc) were separated by SDS-PAGE, blotted, and then probed with E1 antibody.

SUBCELLULAR DISTRIBUTION OF TAU PROTEIN IN JNPL3 MICE

To identify tau protein in a synaptosomal fraction, we first performed subcellular fractionation and organelle enrichment by basic differential centrifugation protocol (30) (**Figure 2A**). As a result, pre-synaptic markers (GAP-43, synaptotagmin) and post-synaptic marker (PSD-95) were mostly distributed in the crude synaptosomal (P2) fraction (**Figure 2B**). Tau was recovered at equal ratios in the nuclear (P1), P2, and cytosolic (S3) fractions (**Figure 2C**). Distributions of tau, β-actin and β-tubulin in each fraction were similar in JNPL3 mice and non-Tg littermates (**Figures 2B,C**). Interestingly, the proportion of the tau level in S3 fraction was significantly lower than that of the β-tubulin level in S3 fraction (**Figure 2C**, tau and β-tubulin in S3 from JNPL3 were 30.2 and 41.7%, respectively, $p < 0.05$; tau and β-tubulin in S3 from non-tg were 31.2 and 44.9%, respectively, $p < 0.01$). This suggests that tau may have distinct functions rather than that of microtubule-association property. To further characterize the synaptosomal fraction, P2 fraction was lysed hypotonically and divided by differential centrifugation to obtain synaptosomal membrane (LP1), synaptic vesicle (LP2), and soluble synaptosomal (LS2) fractions (**Figure 2A**). GAP-43, synaptotagmin, and PSD-95 were mostly distributed in LP1 fraction (**Figure 2B**). Some of the synaptotagmin immunoreactivity was detected in LP2 as a synaptic vesicle protein (**Figure 2B**). Interestingly, abundant levels of both human and mouse tau were detected in LP1 but not in LP2 fraction (**Figure 2B**). Similar to the proportions of tau and β-tubulin S3 fraction, the proportion of the tau level in LP1 fraction was significantly higher than that of the β-tubulin level in LP1 fraction (**Figure 2D**, tau and β-tubulin in LP1 from JNPL3 were 77.9 and 39.4%, respectively, $p < 0.001$; tau and β-tubulin in LP1 from non-tg were 75.1 and 36.0%, respectively, $p < 0.001$). Again, tau may have a function that is not related to the microtubule-association. Furthermore, tau proteins in P1, P2, P3, and LP1 fractions had migrated faster than that in S3 fraction (**Figure 2B**, Tau5 and E1 blots), suggesting that posttranslational modification of those tau proteins was different from that of cytosolic tau protein.

TAU IN SYNAPTOSOMAL FRACTION

To examine the effect of transgenic tau expression in the synaptosomal fraction, we next analyzed the protein property of tau in LP1 fraction. A panel of tau antibodies (E1, Tau5, MS06, Tau1, pS199, pT231, and pS396) confirmed the difference in band pattern between S3 and LP1 fractions (**Figures 3A** and **4A,B**). When tau phosphorylations at the sites of Ser199, Thr231, and Ser396 were compared, those sites in LP1 were less-phosphorylated than in S3 fraction (**Figures 3B,C**). Tau1 antibody confirmed a higher level of de-phosphorylated tau in LP1 fraction than in S3 fraction of both JNPL3 and non-tg mice (**Figures 3B,C**). The ratio of tau phosphorylation between S3 and LP1 fractions of non-Tg mouse brain was similar to that of JNPL3 mouse brain [JNPL3, ratio of LP1/S3 = 1.24 (Tau1), 0.40 (pS199), 0.36 (pT231), 0.42 (pS396); non-tg, ratio of LP1/S3 = 1.16 (Tau1), 0.33 (pS199), 0.36 (pT231), 0.43 (pS396)] (**Figures 3B,C**). Total tau level in LP1 fraction from non-tg mice was also lower than that in S3 fraction

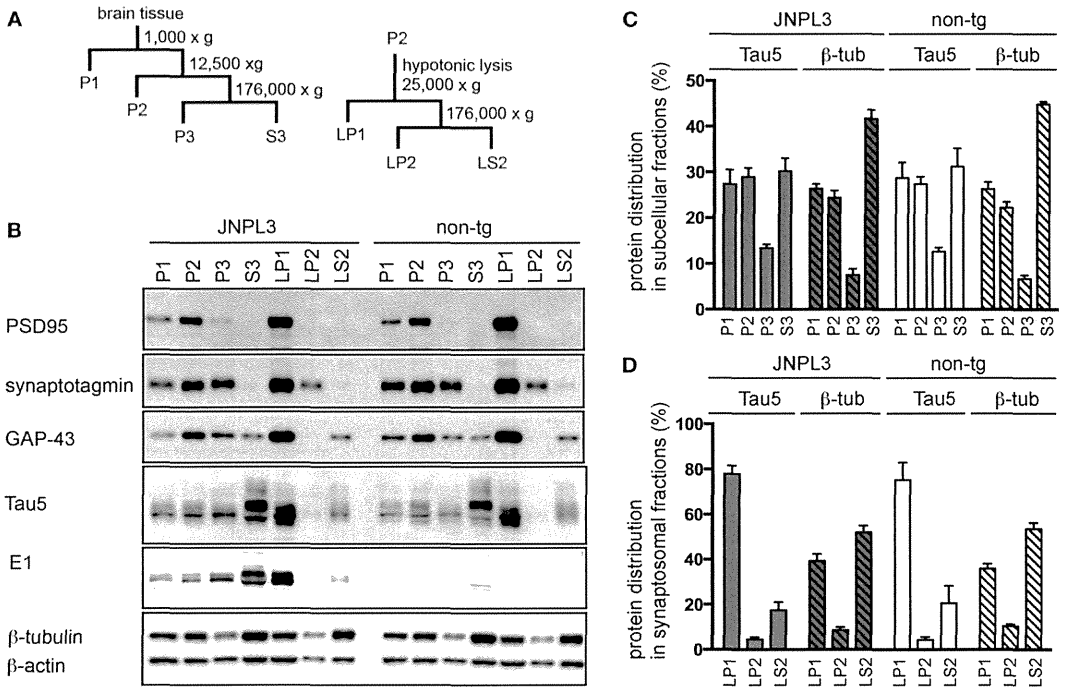

FIGURE 2 | Subcellular fractionation of mouse cerebral cortex. **(A)** Schematic representation of the subcellular fractionation steps. P1, nuclear pellet and debris; P2, crude synaptosomal fraction; P3, light membranes; S3, cytosolic fraction; LP1, synaptosomal membrane fraction; LP2, synaptic vesicle-enriched fraction; LS2, soluble synaptosomal fraction. **(B)** Western blots of JNPL3 and non-tg male mouse cerebral cortex subcellular fractions. P1, P2, P3, or S3 fraction derived from 0.13 mg wet weight of tissue and LP1, LP2, or LS2 fraction derived from 0.5 mg wet weight of tissue were loaded on SDS-PAGE. Blots were probed with PSD-95, synaptotagmin, GAP-43, Tau5, E1, β-tubulin, and β-actin antibodies. **(C)** Proportions of protein levels in fractions (P1, P2, P3, and S3) of tau (Tau5) and β-tubulin (β-tub) from JNPL3 ($n = 5$) and non-tg ($n = 5$) mice are shown. Intensities of tau (49–65 kDa) and β-tubulin (50 kDa) were measured by Bio-Imaging Analyzer System. Ratios were indicated by percent of total (P1 + P2 + P3 + S3). Results are expressed as mean ± SEM. **(D)** Proportions of protein levels in synaptosomal fractions (LP1, LP2, and LS2) of tau (Tau5) and β-tubulin (β-tub) from JNPL3 ($n = 5$) and non-tg ($n = 5$) mice were indicated. Intensities of tau (49–65 kDa) and β-tubulin (50 kDa) were measured by Bio-Imaging Analyzer System. Ratios were indicated by percent of total (LP1 + LP2 + LS2). Results are expressed as mean ± SEM.

[Tau5, LP1/S3 = 0.37] (**Figure 3C**). Although tau phosphorylations at the sites of Ser199, Thr231, and Ser396 in LP1 fraction of JNPL3 mice was clearly less than those in S3 fraction, mouse tau phosphorylation in LP1 fraction might be reduced at a few sites. Further analysis will be needed to determine differential phosphorylation sites in S3 and LP1 fractions of non-tg mice.

In JNPL3 mice, more human P301L mutant tau was detected in LP1 fraction than in S3 fraction (**Figures 3A,B**). In contrast, the total tau level including both human P301L tau and mouse tau was higher in S3 fraction than in LP1 fraction (**Figures 3A,B**). The higher level of human P301L tau was further confirmed by the lower level of mouse tau in LP1 fraction than in S3 fraction as detected by mouse tau-specific tau antibody MS06 (**Figures 3A,B**). These data indicate that the distribution of human P301L tau in the synaptosomal fraction is greater than in the cytosolic fraction while that of mouse tau is greater in the cytosolic fraction than in the synaptosomal fraction. It should be noted that Tau5 immunoreactivity in LP1 fraction of JNPL3 mice was more than twofold that of non-Tg mice (2.6-fold) while Tau5 immunoreactivity in S3 fraction of JNPL3 mice was less than twofold that of non-tg mice (1.3-fold). This further suggests the greater distribution of human P301L tau in LP1 fraction than in S3 fraction. Taken together, our biochemical analysis of the subcellular fraction revealed the existence of transgenic human P301L tau in the synaptosomal fraction with less-phosphorylation.

PHOSPHORYLATED HUMAN P301L TAU IN SYNAPTOSOMAL FRACTION

Although the levels of tau phosphorylation in JNPL3 mice were similar to those in non-tg mice, we compared western blot profiles of tau protein between JNPL3 and non-tg mice. Molecular weights of major tau bands in S3 and LP1 fractions were estimated by protein standard markers (**Figure 4**). In S3 fraction of JNPL3 mice, two bands migrating to 50 and 55 kDa were labeled with tau antibodies E1, Tau5, MS06, pS199, pT231, and pS396 (**Figure 4A**). Tau1 antibody labeled the 50 kDa band but sparsely labeled the 55 kDa band (**Figure 4A**). Blot profiles of JNPL3 mice were not so different from those of non-tg mice (**Figure 4A**). JNPL3 mice expressed both human 4R0N tau isoform and mouse tau isoforms. In addition, it already is known that 4R0N isoform is most expressed in adult mouse brains (33). Therefore, the main components of these two bands might be human and mouse 4R0N tau isoforms, although the possibility of other mouse tau isoforms being induced by exogenous human

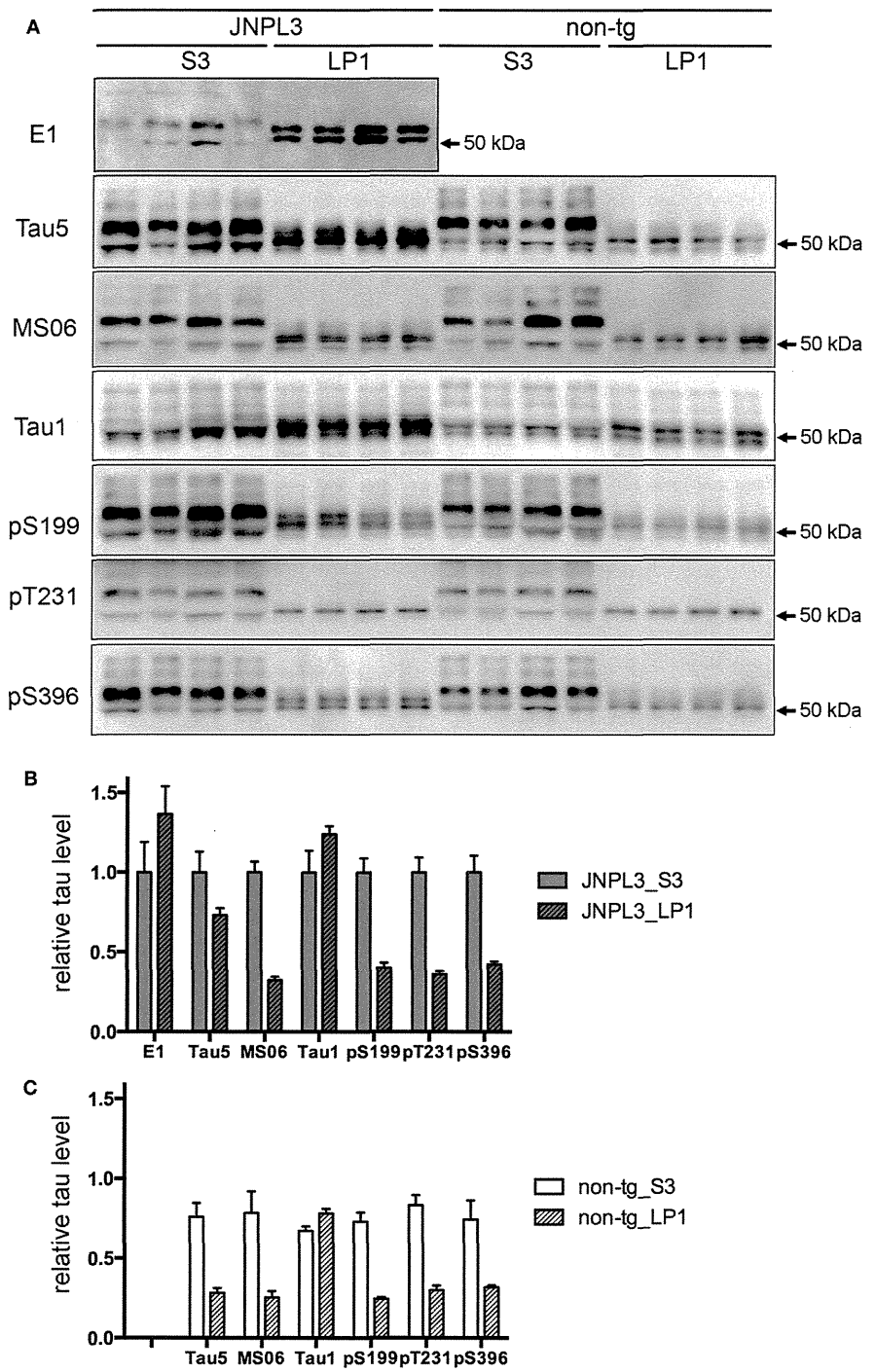

FIGURE 3 | Quantitative western blot analysis of tau protein. **(A)** Tau band patterns in cytosolic (S3) and synaptosomal membrane (LP1) fractions from four JNPL3 and four non-tg mouse cerebral cortices. Equal volumes of fractions derived from 0.25 mg wet weight of brain were separated by SDS-PAGE, blotted, and then probed with Tau5, MS06, Tau1, pS199, pT231, and pS396 antibodies. **(B,C)** The relative ratio of tau protein between S3 and LP1 fractions from JNPL3 **(B)** and non-tg **(C)** mice was measured ($n = 4$ each). Results are expressed as mean ± SEM. The mean value of tau protein in S3 fraction from JNPL3 mice was normalized to one.

tau cannot be excluded. In LP1 fraction, human tau appeared with 51 and 53 kDa bands (**Figure 4B**, E1 blot) whereas mouse tau appeared on 49 and 51 kDa bands (**Figure 4B**, MS06 blots). This phenomenon was also seen in blots of pS199 and pS396 antibodies (**Figure 4B**, 51 and 53 kDa bands in JNPL3, and 49 and 51 kDa bands in non-tg). The 53 kDa band was labeled with E1,

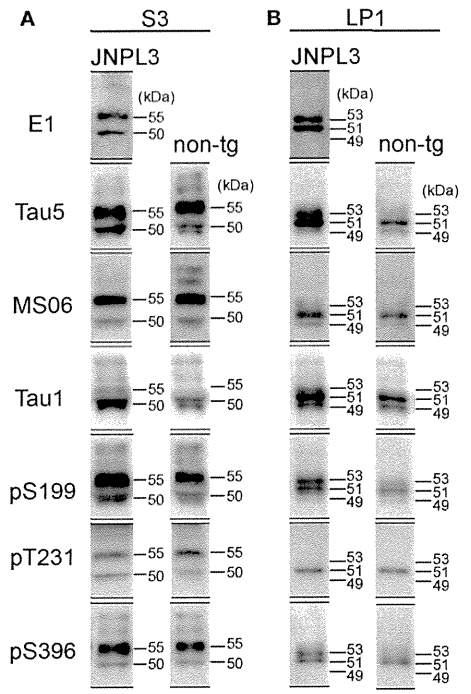

FIGURE 4 | Comparison of western blot profiles between JNPL3 and non-tg mice. (A) Representative blots of S3 fraction stained by tau antibodies (E1, Tau5, MS06, Tau1, pS199, pT231, and pS396). Molecular weights were determined by reference standard markers. Two major bands were migrated to 50 and 55 kDa. Except Tau1 antibody, the 55 kDa band was more intensely stained than 50 kDa band. **(B)** Representative blots of LP1 fraction stained by tau antibodies (E1, Tau5, MS06, Tau1, pS199, pT231, and pS396). In JNPL3 mouse, two major bands appeared with slower migration (53 kDa) and faster migration (51 kDa) in E1, Tau5, pS199, and pS396 blots. Two bands appeared on 49 and 51 kDa in MS06 blot. Three bands (49, 51, and 53 kDa) appeared in Tau1 blot. Only 51 kDa band appeared in pT231 blot. In non-tg mouse, 49 and 51 kDa bands appeared in Tau5, MS06, and Tau1 blots. Three bands (49, 51, and 53 kDa) appeared in pS199 blot. Only 51 kDa band appeared in pT231 and pS396 blots.

Tau5, Tau1, pS199, and pS396 antibodies, but not with MS06 and pT231 antibodies. Because of slower mobility in SDS-PAGE, we expected the 53 kDa band to be more phosphorylated than the 51 kDa band. However, the same size of band was labeled with Tau1 antibody and not labeled with pT231 antibody, indicating that this 53 kDa band contained both phosphorylated tau at Ser199 and Ser396 and non-phosphorylated tau at Ser199 and Thr231. In addition, because the molecular size was quite different from the hyperphosphorylated 64 kDa tau (**Figure 1B**), the 53 kDa band was unlikely to be hyperphosphorylated. Regardless, identification of phosphorylation sites and tau isoforms will be necessary to determine the status of tau phosphorylation and expression in LP1 fraction.

DISCUSSION

Transgenic mouse models of human neurodegenerative diseases have been developed with the aim of reproducing the histopathological hallmarks of human diseases. For this purpose, neuropathology and biochemistry were commonly used for the definition of disease progress. Previous studies expressing transgenic tau under the control of neuronal promoters have successfully shown neuropathological hallmarks with the appearance of motor impairment (28, 34, 35). However, the phenotype did not completely match with AD because none of these tau transgenic lines had been comprehensively evaluated in terms of cognitive performance. Recently, rTg4510 mice were examined for the association of NFT formation with cognitive function, demonstrating that suppression of P301L tau expression reversed behavioral impairments although NFT formation continued (9). In rTg4510 mice and a neuronal cell culture model of tauopathy, the mislocalization of tau to dendritic spines was examined (16). Moreover, a novel function of tau altering Fyn kinase-mediated NMDA stabilization was reported (17, 21). However, it is still unclear whether abnormally hyperphosphorylated tau is accumulated in post-synaptic regions while having a function of NMDA stabilization. In the present study, instead of using a mouse model with extremely high expression of P301L tau, 15- to 18-month-old male JNPL3 mice were examined for their synaptosomal tau distribution. As previously reported (32), the hyperphosphorylated 64 kDa tau was barely detectable in the sarkosyl-insoluble fraction from male JNPL3 mice with a C57BL/6J strain background. Therefore, our biochemical analysis was unable to determine whether the hyperphosphorylated tau was distributed in synaptosomal fractions. However, we observed that less-phosphorylated tau was recovered in the synaptosomal fraction and that tau distribution was induced by exogenous human P301L tau expression. Interestingly, the sarkosyl-insoluble fraction extracted from male JNPL3 mice contained similar less-phosphorylated tau proteins (**Figure 1B**). It may be possible that transition from less-phosphorylation to hyperphosphorylation takes place in synaptic regions. Further study will be needed to confirm this possibility.

Among the cytoskeletal proteins showing polarized distribution, tau is abundantly localized in axons (27, 36–40). Therefore, it is reasonable to assume that the distribution of tau protein reaches the axon terminal. In fact, Fein et al. confirmed this by a flow cytometry method for detecting tau protein in synapses in AD brain (41). Here, we also showed significant amounts of tau protein in the synaptosomal fraction by using a subcellular fractionation method. Interestingly, the tau protein in this fraction was less-phosphorylated than that in the cytosolic fraction. Our quantitative analysis revealed that non-phosphorylated tau at Ser199 (detected by Tau1 antibody), as well as transgenic P301L mutant human tau, was distributed in the synaptosomal fraction. It was reported that the selective binding of tau to axonal microtubules was regulated by phosphorylation, as tau in axons was mostly stained by Tau1 antibody whereas tau in the cell body and dendrites was stained by AT8 antibody (42). Therefore, we speculated that P301L mutant human tau was functionally localized in the axon terminal with less-phosphorylation. In our synaptosome preparation with hypotonic lysis, tau was mostly recovered in the synaptosomal membrane fraction. As about 25% of cellular tau is reportedly located in membrane fractions (43), it is quite likely that tau exists in synapse in association with synaptosomal membrane components. At least, we know that tau can associate with various other proteins in addition

to tubulin, including the SH3 domains of Src family tyrosine kinase (44). Because the synaptosomal membrane fraction contained more Tau1-positive tau than phosphorylated tau, most tau protein may localize in pre-synaptic regions. In contrast, localization of tau in dendritic spines was confirmed by the use of co-immunoprecipitation with PSD complex (17) and immunocytochemistry of EGFP-tagged tau expression in primary neuronal culture (16). In 12-month-old rTg4510 mice, a significant decrease in the synaptic protein level was biochemically demonstrated (20). These data strongly suggest that tau plays a critical role in the post-synaptic region in spite of the fact that the existence of hyperphosphorylated 64 kDa tau in dendritic spines of rTg4510 mice has not yet been conclusively proven. On the other hand, recent studies clarified that microtubule dynamics are essential for the regulation of spine morphology (45–47). Microtubule incursions into spines have been demonstrated in mature hippocampal cultures, suggesting that tau can be released at the plus-end of microtubules in spine. It was also reported that microtubule affinity-regulating kinase is essential for maintaining spine morphology (48). Therefore, the search for a transition mechanism of tau into the post-synaptic region is a project of major interest.

In conclusion, we observed that tau in the synaptosomal fraction was less-phosphorylated than that in the cytosolic fraction, and that synaptosomal tau distribution was induced by overexpression of human P301L tau in a transgenic mouse model of tauopathy. Although our data cannot determine whether the detected tau is of pre-synaptic or post-synaptic origin, further investigations will allow us to elucidate the critical role of tau in synapse. Regulating the synaptosomal tau level might be a target for therapeutic interventions to protect the formation of toxic tau species inducing synaptic dysfunction.

ACKNOWLEDGMENTS

The authors thank Dr. Miyasaka Tomohiro (Doshisha University) for providing the polyclonal anti-mouse tau antibody MS06, and Dr. P. Davies (Albert Einstein University, Bronx, NY, USA) for the monoclonal anti-tau antibody PHF1. This research was supported by research grants from RIKEN BSI, and Grants-in-Aid for Japan Advanced Molecular Imaging Program and Science Research (Japan Ministry of Education, Science, Sports and Culture).

REFERENCES

1. Lee VM, Goedert M, Trojanowski JQ. Neurodegenerative tauopathies. *Annu Rev Neurosci* (2001) **24**:1121–59. doi:10.1146/annurev.neuro.24.1.1121
2. Swaab DF, Dubelaar EJ, Hofman MA, Scherder EJ, Van Someren EJ, Verwer RW. Brain aging and Alzheimer's disease; use it or lose it. *Prog Brain Res* (2002) **138**:343–73. doi:10.1016/S0079-6123(02)38086-5
3. Binder LI, Guillozet-Bongaarts AL, Garcia-Sierra F, Berry RW. Tau, tangles, and Alzheimer's disease. *Biochim Biophys Acta* (2005) **1739**:216–23. doi:10.1016/j.bbadis.2004.08.014
4. Gomez-Isla T, Hollister R, West H, Mui S, Growdon JH, Petersen RC, et al. Neuronal loss correlates with but exceeds neurofibrillary tangles in Alzheimer's disease. *Ann Neurol* (1997) **41**:17–24. doi:10.1002/ana.410410106
5. Goedert M, Spillantini MG. Tau mutations in frontotemporal dementia FTDP-17 and their relevance for Alzheimer's disease. *Biochim Biophys Acta* (2000) **1502**:110–21. doi:10.1016/S0925-4439(00)00037-5
6. Hutton M. Molecular genetics of chromosome 17 tauopathies. *Ann N Y Acad Sci* (2000) **920**:63–73. doi:10.1111/j.1749-6632.2000.tb06906.x
7. Spillantini MG, Van Swieten JC, Goedert M. Tau gene mutations in frontotemporal dementia and parkinsonism linked to chromosome 17 (FTDP-17). *Neurogenetics* (2000) **2**:193–205. doi:10.1007/s100489900084
8. Reed LA, Wszolek ZK, Hutton M. Phenotypic correlations in FTDP-17. *Neurobiol Aging* (2001) **22**:89–107. doi:10.1016/S0197-4580(00)00202-5
9. Santacruz K, Lewis J, Spires T, Paulson J, Kotilinek L, Ingelsson M, et al. Tau suppression in a neurodegenerative mouse model improves memory function. *Science* (2005) **309**:476–81. doi:10.1126/science.1113694
10. Augustinack JC, Schneider A, Mandelkow EM, Hyman BT. Specific tau phosphorylation sites correlate with severity of neuronal cytopathology in Alzheimer's disease. *Acta Neuropathol* (2002) **103**:26–35. doi:10.1007/s004010100423
11. Kopke E, Tung YC, Shaikh S, Alonso AC, Iqbal K, Grundke-Iqbal I. Microtubule-associated protein tau. Abnormal phosphorylation of a non-paired helical filament pool in Alzheimer disease. *J Biol Chem* (1993) **268**:24374–84.
12. Berger Z, Roder H, Hanna A, Carlson A, Rangachari V, Yue M, et al. Accumulation of pathological tau species and memory loss in a conditional model of tauopathy. *J Neurosci* (2007) **27**:3650–62. doi:10.1523/JNEUROSCI.0587-07.2007
13. Lasagna-Reeves CA, Castillo-Carranza DL, Sengupta U, Sarmiento J, Troncoso J, Jackson GR, et al. Identification of oligomers at early stages of tau aggregation in Alzheimer's disease. *FASEB J* (2012) **26**:1946–59. doi:10.1096/fj.11-199851
14. Ren Y, Sahara N. Characteristics of tau oligomers. *Front Neurol* (2013) **4**:102. doi:10.3389/fneur.2013.00102
15. Sahara N, Deture M, Ren Y, Ebrahim A-S, Kang D, Knight J, et al. Characteristics of TBS-extractable hyperphosphorylated Tau species: aggregation intermediates in rTg4510 mouse brain. *J Alzheimers Dis* (2013) **33**:249–63. doi:10.3233/JAD-2012-121093
16. Hoover BR, Reed MN, Su J, Penrod RD, Kotilinek LA, Grant MK, et al. Tau mislocalization to dendritic spines mediates synaptic dysfunction independently of neurodegeneration. *Neuron* (2010) **68**:1067–81. doi:10.1016/j.neuron.2010.11.030
17. Ittner LM, Ke YD, Delerue F, Bi M, Gladbach A, Van Eersel J, et al. Dendritic function of tau mediates amyloid-beta toxicity in Alzheimer's disease mouse models. *Cell* (2010) **142**:387–97. doi:10.1016/j.cell.2010.06.036
18. Zempel H, Thies E, Mandelkow E, Mandelkow EM. Abeta oligomers cause localized Ca(2+) elevation, missorting of endogenous Tau into dendrites, Tau phosphorylation, and destruction of microtubules and spines. *J Neurosci* (2010) **30**:11938–50. doi:10.1523/JNEUROSCI.2357-10.2010
19. Larson M, Sherman MA, Amar F, Nuvolone M, Schneider JA, Bennett DA, et al. The complex PrP(c)-Fyn couples human oligomeric Abeta with pathological tau changes in Alzheimer's disease. *J Neurosci* (2012) **32**:16857–71. doi:10.1523/JNEUROSCI.1858-12.2012
20. Kopeikina KJ, Polydoro M, Tai HC, Yaeger E, Carlson GA, Pitstick R, et al. Synaptic alterations in the rTg4510 mouse model of tauopathy. *J Comp Neurol* (2013) **521**:1334–53. doi:10.1002/cne.23234
21. Roberson ED, Halabisky B, Yoo JW, Yao J, Chin J, Yan F, et al. Amyloid-beta/Fyn-induced synaptic, network, and cognitive impairments depend on tau levels in multiple mouse models of Alzheimer's disease. *J Neurosci* (2011) **31**:700–11. doi:10.1523/JNEUROSCI.4152-10.2011
22. Trinczek B, Ebneth A, Mandelkow EM, Mandelkow E. Tau regulates the attachment/detachment but not the speed of motors in microtubule-dependent transport of single vesicles and organelles. *J Cell Sci* (1999) **112**(Pt 14):2355–67.
23. Ebneth A, Godemann R, Stamer K, Illenberger S, Trinczek B, Mandelkow E. Overexpression of tau protein inhibits kinesin-dependent trafficking of vesicles, mitochondria, and endoplasmic reticulum: implications for Alzheimer's disease. *J Cell Biol* (1998) **143**:777–94. doi:10.1083/jcb.143.3.777
24. Seitz A, Kojima H, Oiwa K, Mandelkow EM, Song YH, Mandelkow E. Single-molecule investigation of the interference between kinesin, tau and MAP2c. *EMBO J* (2002) **21**:4896–905. doi:10.1093/emboj/cdf503
25. Stamer K, Vogel R, Thies E, Mandelkow E, Mandelkow EM. Tau blocks traffic of organelles, neurofilaments, and APP vesicles in neurons and enhances oxidative stress. *J Cell Biol* (2002) **156**:1051–63. doi:10.1083/jcb.200108057
26. Santarella RA, Skiniotis G, Goldie KN, Tittmann P, Gross H, Mandelkow EM, et al. Surface-decoration of microtubules by human tau. *J Mol Biol* (2004) **339**:539–53. doi:10.1016/j.jmb.2004.04.008
27. Binder LI, Frankfurter A, Rebhun LI. The distribution of tau in the mammalian central nervous system. *J Cell Biol* (1985) **101**:1371–8. doi:10.1083/jcb.101.4.1371

28. Lewis J, Mcgowan E, Rockwood J, Melrose H, Nacharaju P, Van Slegtenhorst M, et al. Neurofibrillary tangles, amyotrophy and progressive motor disturbance in mice expressing mutant (P301L) tau protein. *Nat Genet* (2000) **25**:402–5. doi:10.1038/78078
29. Sahara N, Lewis J, Deture M, Mcgowan E, Dickson DW, Hutton M, et al. Assembly of tau in transgenic animals expressing P301L tau: alteration of phosphorylation and solubility. *J Neurochem* (2002) **83**:1498–508. doi:10.1046/j.1471-4159.2002.01241.x
30. Niethammer M, Smith DS, Ayala R, Peng J, Ko J, Lee MS, et al. NUDEL is a novel Cdk5 substrate that associates with LIS1 and cytoplasmic dynein. *Neuron* (2000) **28**:697–711. doi:10.1016/S0896-6273(00)00147-I
31. Kenessey A, Nacharaju P, Ko LW, Yen SH. Degradation of tau by lysosomal enzyme cathepsin D: implication for Alzheimer neurofibrillary degeneration. *J Neurochem* (1997) **69**:2026–38. doi:10.1046/j.1471-4159.1997.69052026.x
32. Bolmont T, Clavaguera F, Meyer-Luehmann M, Herzig MC, Radde R, Staufenbiel M, et al. Induction of tau pathology by intracerebral infusion of amyloid-beta -containing brain extract and by amyloid-beta deposition in APP x Tau transgenic mice. *Am J Pathol* (2007) **171**:2012–20. doi:10.2353/ajpath.2007.070403
33. Takuma H, Arawaka S, Mori H. Isoforms changes of tau protein during development in various species. *Brain Res Dev Brain Res* (2003) **142**:121–7. doi:10.1016/S0165-3806(03)00056-7
34. Allen B, Ingram E, Takao M, Smith MJ, Jakes R, Virdee K, et al. Abundant tau filaments and nonapoptotic neurodegeneration in transgenic mice expressing human P301S tau protein. *J Neurosci* (2002) **22**:9340–51.
35. Terwel D, Lasrado R, Snauwaert J, Vandeweert E, Van Haesendonck C, Borghgraef P, et al. Changed conformation of mutant Tau-P301L underlies the moribund tauopathy, absent in progressive, nonlethal axonopathy of Tau-4R/2N transgenic mice. *J Biol Chem* (2005) **280**:3963–73. doi:10.1074/jbc.M409876200
36. Peng I, Binder LI, Black MM. Biochemical and immunological analyses of cytoskeletal domains of neurons. *J Cell Biol* (1986) **102**:252–62. doi:10.1083/jcb.102.1.252
37. Kosik KS, Finch EA. MAP2 and tau segregate into dendritic and axonal domains after the elaboration of morphologically distinct neurites: an immunocytochemical study of cultured rat cerebrum. *J Neurosci* (1987) **7**:3142–53.
38. Brion JP, Guilleminot J, Couchie D, Flament-Durand J, Nunez J. Both adult and juvenile tau microtubule-associated proteins are axon specific in the developing and adult rat cerebellum. *Neuroscience* (1988) **25**:139–46. doi:10.1016/0306-4522(88)90013-9
39. Mandell JW, Banker GA. The microtubule cytoskeleton and the development of neuronal polarity. *Neurobiol Aging* (1995) **16**:229–37. doi:10.1016/0197-4580(94)00164-V discussion 238,
40. Hirokawa N, Funakoshi T, Sato-Harada R, Kanai Y. Selective stabilization of tau in axons and microtubule-associated protein 2C in cell bodies and dendrites contributes to polarized localization of cytoskeletal proteins in mature neurons. *J Cell Biol* (1996) **132**:667–79. doi:10.1083/jcb.132.4.667
41. Fein JA, Sokolow S, Miller CA, Vinters HV, Yang F, Cole GM, et al. Co-localization of amyloid beta and tau pathology in Alzheimer's disease synaptosomes. *Am J Pathol* (2008) **172**:1683–92. doi:10.2353/ajpath.2008.070829
42. Kanai Y, Hirokawa N. Sorting mechanisms of tau and MAP2 in neurons: suppressed axonal transit of MAP2 and locally regulated microtubule binding. *Neuron* (1995) **14**:421–32. doi:10.1016/0896-6273(95)90298-8
43. Maas T, Eidenmuller J, Brandt R. Interaction of tau with the neural membrane cortex is regulated by phosphorylation at sites that are modified in paired helical filaments. *J Biol Chem* (2000) **275**:15733–40. doi:10.1074/jbc.M000389200
44. Reynolds CH, Garwood CJ, Wray S, Price C, Kellie S, Perera T, et al. Phosphorylation regulates tau interactions with Src homology 3 domains of phosphatidylinositol 3-kinase, phospholipase Cgamma1, Grb2, and Src family kinases. *J Biol Chem* (2008) **283**:18177–86. doi:10.1074/jbc.M709715200
45. Gu J, Firestein BL, Zheng JQ. Microtubules in dendritic spine development. *J Neurosci* (2008) **28**:12120–4. doi:10.1523/JNEUROSCI.2509-08.2008
46. Hu X, Viesselmann C, Nam S, Merriam E, Dent EW. Activity-dependent dynamic microtubule invasion of dendritic spines. *J Neurosci* (2008) **28**:13094–105. doi:10.1523/JNEUROSCI.3074-08.2008
47. Jaworski J, Kapitein LC, Gouveia SM, Dortland BR, Wulf PS, Grigoriev I, et al. Dynamic microtubules regulate dendritic spine morphology and synaptic plasticity. *Neuron* (2009) **61**:85–100. doi:10.1016/j.neuron.2008.11.013
48. Hayashi K, Suzuki A, Hirai S, Kurihara Y, Hoogenraad CC, Ohno S. Maintenance of dendritic spine morphology by partitioning-defective 1b through regulation of microtubule growth. *J Neurosci* (2011) **31**:12094–103. doi:10.1523/JNEUROSCI.0751-11.2011

Conflict of Interest Statement: The authors declare that the research was conducted in the absence of any commercial or financial relationships that could be construed as a potential conflict of interest.

Received: 14 December 2013; accepted: 24 February 2014; published online: 11 March 2014.

Citation: Sahara N, Murayama M, Higuchi M, Suhara T and Takashima A (2014) Biochemical distribution of tau protein in synaptosomal fraction of transgenic mice expressing human P301L tau. Front. Neurol. 5:26. doi: 10.3389/fneur.2014.00026

This article was submitted to Neurodegeneration, a section of the journal Frontiers in Neurology.

Eur J Nucl Med Mol Imaging (2014) 41:745–754
DOI 10.1007/s00259-013-2620-7

ORIGINAL ARTICLE

Imaging of amyloid deposition in human brain using positron emission tomography and [^{18}F]FACT: comparison with [^{11}C] PIB

Hiroshi Ito · Hitoshi Shinotoh · Hitoshi Shimada · Michie Miyoshi · Kazuhiko Yanai · Nobuyuki Okamura · Harumasa Takano · Hidehiko Takahashi · Ryosuke Arakawa · Fumitoshi Kodaka · Maiko Ono · Yoko Eguchi · Makoto Higuchi · Toshimitsu Fukumura · Tetsuya Suhara

Received: 14 August 2013 / Accepted: 18 October 2013 / Published online: 14 November 2013

Abstract
Purpose The characteristic neuropathological changes in Alzheimer's disease (AD) are deposition of amyloid senile plaques and neurofibrillary tangles. The ^{18}F-labeled amyloid tracer, [^{18}F]2-[(2-{(E)-2-[2-(dimethylamino)-1,3-thiazol-5-yl]vinyl}-1,3-benzoxazol-6-yl)oxy]-3-fluoropropan-1-ol (FACT), one of the benzoxazole derivatives, was recently developed. In the present study, deposition of amyloid senile plaques was measured by positron emission tomography (PET) with both [^{11}C]Pittsburgh compound B (PIB) and [^{18}F]FACT in the same subjects, and the regional uptakes of both radiotracers were directly compared.
Methods Two PET scans, one of each with [^{11}C]PIB and [^{18}F]FACT, were performed sequentially on six normal control subjects, two mild cognitive impairment (MCI) patients, and six AD patients. The standardized uptake value ratio of brain regions to the cerebellum was calculated with partial volume correction using magnetic resonance (MR) images to remove the effects of white matter accumulation.
Results No significant differences in the cerebral cortical uptake were observed between normal control subjects and AD patients in [^{18}F]FACT studies without partial volume correction, while significant differences were observed in [^{11}C]PIB. After partial volume correction, the cerebral cortical uptake was significantly larger in AD patients than in normal control subjects for [^{18}F]FACT studies as well as [^{11}C]PIB. Relatively lower uptakes of [^{11}C]PIB in distribution were observed in the medial side of the temporal cortex and in the occipital cortex as compared with [^{18}F]FACT. Relatively higher uptake of [^{11}C]PIB in distribution was observed in the frontal and parietal cortices.
Conclusion Since [^{18}F]FACT might bind more preferentially to dense-cored amyloid deposition, regional differences in cerebral cortical uptake between [^{11}C]PIB and [^{18}F]FACT might be due to differences in regional distribution between diffuse and dense-cored amyloid plaque shown in the autoradiographic and histochemical assays of postmortem AD brain sections.

Keywords Amyloid · Alzheimer · PET · FACT · PIB

H. Ito · H. Shinotoh · H. Shimada · M. Miyoshi · H. Takano · H. Takahashi · R. Arakawa · F. Kodaka · M. Ono · Y. Eguchi · M. Higuchi · T. Fukumura · T. Suhara
Molecular Imaging Center, National Institute of Radiological Sciences, Chiba, Japan

K. Yanai · N. Okamura
Department of Pharmacology, Tohoku University School of Medicine, Sendai, Japan

H. Ito (✉)
Biophysics Program, Molecular Imaging Center, National Institute of Radiological Sciences, 4-9-1 Anagawa, Inage-ku, Chiba 263-8555, Japan
e-mail: hito@nirs.go.jp

Introduction

Alzheimer's disease (AD) is the most common neurodegenerative dementia, and the characteristic neuropathological

changes in AD are deposition of amyloid senile plaques and neurofibrillary tangles (NFTs) [1]. The amyloid cascade hypothesis that deposition of amyloid protein would cause Alzheimer's pathology, e.g., the NFTs, cell loss, and vascular damage as a direct result of this deposition, has been proposed [2], and in vivo imaging of the deposition of amyloid senile plaques should contribute to the early diagnosis and evaluation for the treatment of AD. Several radiotracers to measure deposition of amyloid senile plaques by positron emission tomography (PET), e.g., [^{11}C]Pittsburgh compound B (PIB) [3, 4], [^{18}F]FDDNP [5], [^{11}C]SB-13 [6], [^{11}C]BF227 [7], [^{18}F]BAY94-9172 [8], [^{18}F]AV-45 [9], [^{11}C]AZD2184 [10], and [^{18}F]AZD4694 [11], were developed and used for investigation of the pathophysiology of AD.

[^{11}C]PIB, a benzothiazole derivative, is the most successful radiotracer for amyloid imaging and is widely used for clinical research of AD [12, 13]. However, cortical uptake of [^{11}C]PIB was often observed in healthy subjects with normal neuropsychological findings [14]. Since the fraction of soluble amyloid deposition in normal brain has been reported to be larger than that in AD brain [15], the cortical uptake of [^{11}C]PIB in normal subjects might be mainly due to binding to diffuse amyloid plaque.

Recently, [^{11}C]BF227, a benzoxazole derivative, was developed for in vivo imaging of amyloid senile plaques [7]. This radiotracer has been considered to bind more preferentially to dense-cored amyloid deposition than [^{11}C]PIB. It has been reported that synapse loss was accentuated within immature and mature plaques, but not within diffuse plaques [16], and the neuropathology of AD is characterized by cortical neuritic plaque containing dense-cored amyloid deposition [17]. Thus, a selective radiotracer for neuritic amyloid plaque might be useful for distinguishing the normal aging process from AD.

The ^{18}F-labeled amyloid tracer, [^{18}F]2-[(2-{(E)-2-[2-(dimethylamino)-1,3-thiazol-5-yl]vinyl}-1,3-benzoxazol-6-yl)oxy]-3-fluoropropan-1-ol (fluorinated amyloid imaging compound of Tohoku University, [^{18}F]FACT), one of the benzoxazole derivatives with a structure similar to [^{11}C]BF227, was recently developed [18, 19]. For [^{18}F]FACT, rapid accumulation and rapid washout were observed in the brains of both normal control subjects and AD patients, indicating its suitability as an amyloid imaging tracer in PET measurements [18]. Regional distribution similar to that of [^{11}C]BF227 was also observed. In the present study, deposition of amyloid senile plaques was measured by PET with both [^{11}C]PIB and [^{18}F]FACT in the same subjects including normal control subjects, mild cognitive impairment (MCI) patients, and AD patients. The binding and regional distribution of both radiotracers were directly compared to elucidate the binding characteristics of [^{18}F]FACT. To identify pathological aggregates providing major binding components for [^{11}C]PIB and [^{18}F]FACT, comparative autoradiographic and histochemical assays of postmortem AD brain sections were also performed.

Materials and methods

Subjects

Six normal control subjects (50–74 years old), two MCI patients (69 and 77 years old), and six AD patients (70–81 years old) were recruited (Table 1). All AD patients were diagnosed according to the National Institute of Neurological and Communicative Diseases and Stroke/Alzheimer's Disease and Related Disorders Association (NINCDS-ADRDA) criteria [20]. All subjects were classified according to the Clinical Dementia Rating (CDR) scale [21]. The normal control subjects corresponded to 0, the MCI patients to 0.5, and the AD subjects to 0.5, 1, or 2 on the CDR scale. The Mini-Mental State Examination (MMSE) was performed for all subjects [22]. No subjects had notable organic lesions in the brain according to magnetic resonance (MR) imaging. The normal control subjects were cognitively unimpaired and free from medications having central nervous action. The study was approved by the Ethics and Radiation Safety Committees of the National Institute of Radiological Sciences, Chiba, Japan. Written informed consent was obtained from all subjects or from their spouses or other close family members.

PET procedures

All PET studies were performed with SET-3000GCT/X (Shimadzu Corp., Kyoto, Japan) [23], which provides 99

Table 1 Profiles of subjects

Subject group	Subject no.	Age (years)	Sex	MMSE score
Normal control	NC1	70	F	29
	NC2	73	M	29
	NC3	74	M	29
	NC4	50	M	28
	NC5	61	M	28
	NC6	67	F	30
MCI	MCI1	77	F	26
	MCI2	69	M	24
AD	AD1	76	F	12
	AD2	71	M	19
	AD3	81	F	19
	AD4	70	F	15
	AD5	76	F	22
	AD6	80	F	24

sections with an axial field of view of 26 cm. Intrinsic spatial resolution was 3.4 mm in-plane and 5.0 mm full-width at half-maximum (FWHM) axially. With a Gaussian filter (cutoff frequency: 0.3 cycle/pixel), the reconstructed in-plane resolution was 7.5 mm FWHM. Data were acquired in three-dimensional mode. Scatter correction was done by a hybrid scatter correction method based on acquisition with a dual-energy window setting [24]. A 4-min transmission scan using a ^{137}Cs line source was performed for correction of attenuation.

Two PET scans, one each with [^{11}C]PIB and [^{18}F]FACT, were performed sequentially. After intravenous rapid bolus injection of [^{11}C]PIB, dynamic PET scanning was performed for 70 min. Then, 50 min after the end of the [^{11}C]PIB PET measurement, dynamic PET scanning was performed for 60 min after intravenous rapid bolus injection of [^{18}F]FACT. The frame sequence consisted of six 10-s frames, three 20-s frames, two 1-min frames, two 3-min frames, and twelve 5-min frames for [^{11}C]PIB and six 10-s frames, three 20-s frames, two 1-min frames, two 3-min frames, and ten 5-min frames for [^{18}F]FACT. Injected radioactivity was 332–493 MBq and 160–233 MBq for [^{11}C]PIB and [^{18}F]FACT, respectively. Specific radioactivity was 51–134 GBq/μmol and 59–494 GBq/μmol for [^{11}C]PIB and [^{18}F]FACT, respectively. [^{18}F]FACT was produced according to the literature [18].

MR imaging procedures

All MR imaging studies were performed with a 1.5-T MR scanner (Philips Medical Systems, Best, The Netherlands). Three-dimensional volumetric acquisition of a T1-weighted gradient echo sequence produced a gapless series of thin transverse sections (echo time 9.2 ms, repetition time 21 ms, flip angle 30°, field of view 256 mm, acquisition matrix 256× 256, slice thickness 1 mm).

Calculation of parametric images

For both [^{11}C]PIB and [^{18}F]FACT studies, standardized uptake value (SUV) images were calculated from time-integrated radioactivity images by normalizing tissue radioactivity concentration with injected dose per body weight. The integration intervals were 50–70 min and 40–60 min for [^{11}C]PIB and [^{18}F]FACT, respectively. Since the cerebellum can be used as a reference brain region lacking fibrillar amyloid plaques [7, 25], the SUV ratio (SUVR) images, indicating amyloid deposition, were calculated as follows:

$$SUVR = SUV_{brain}/SUV_{cerebellum} \quad (1)$$

where SUV_{brain} and $SUV_{cerebellum}$ are SUV in brain regions and the cerebellum, respectively. Although the integration interval of 30–40 min including the peak equilibrium [26] was used for calculation of SUVR in the previous report with [^{18}F]FACT, they showed that almost the same SUVR could be obtained using the integration interval of 40–60 min corresponding to the late time phase after injection of [^{18}F]FACT [18]. Thus, the integration intervals corresponding to the late time phase were used for both [^{11}C]PIB and [^{18}F]FACT in the present study.

Data analysis

All MR images were coregistered to the PET images with the Statistical Parametric Mapping (SPM2) system [27]. MR images were transformed into standard brain size and shape by linear and nonlinear parameters by SPM2 (anatomic standardization). The brain templates used in SPM2 for anatomic standardization were T1 templates for MR images, i.e., Montreal Neurological Institute (MNI)/International Consortium for Brain Mapping (ICBM) 152 T1 templates as supplied with SPM2. All PET images were also transformed into standard brain size and shape by using the same parameters as the MR images. Thus, brain images of all subjects had the same anatomic format. Gray matter, white matter, and cerebrospinal fluid images were segmented and extracted from all anatomically standardized MR images by applying voxel-based morphometry methods with the SPM2 system [28]. These segmented MR images indicate the tissue fraction of gray or white matter per voxel (ml/ml). All anatomically standardized PET, gray matter, and white matter images were smoothed with an 8-mm FWHM isotropic Gaussian kernel, because final spatial resolution of the PET camera was approximately 8 mm FWHM.

Regions of interest (ROIs) were drawn on all anatomically standardized PET, gray matter, and white matter images with reference to the T1-weighted MR image. Elliptical ROIs (8× 32 mm) were defined for the cerebellar cortex, parahippocampal gyrus including hippocampus, posterior region of the cingulate gyrus, base sides of frontal cortex, lateral side of temporal cortex, parietal cortex, cuneus of occipital cortex, and centrum semiovale.

Partial volume correction

SUV values are affected by the nonspecific accumulation of radiotracer in white matter because of the limited spatial resolution of the PET scanner. The SUV values per gray matter fraction in an ROI for cerebral cortical regions were calculated. The SUV value in an ROI can be expressed as follows [29, 30]:

$$SUV = SUV_{gray} \cdot TF_{gray} + SUV_{white} \cdot TF_{white} \quad (2)$$

where SUV_{gray} and SUV_{white} are SUV in gray and white matter, respectively, and TF_{gray} and TF_{white} are the tissue fraction of gray and white matter (ml/ml), respectively. According to this equation, if SUV_{white} is given, SUV_{gray} can be calculated for a given TF_{gray} and TF_{white}, which are determined by voxel-based morphometry with MR imaging. To correct effects of spill-in and spillover of radioactivity between gray and white matter, gray and white matter images smoothed with an 8-mm FWHM isotropic Gaussian kernel almost the same as the final spatial resolution of the PET camera were used for this partial volume correction. In the present study, the SUV_{gray} values were calculated by assuming SUV_{white} to be equal to the SUV value in the centrum semiovale. From the SUV_{gray} values in brain regions and the cerebellum, SUVR values in gray matter ($SUVR_{gray}$) were calculated by Eq. 1.

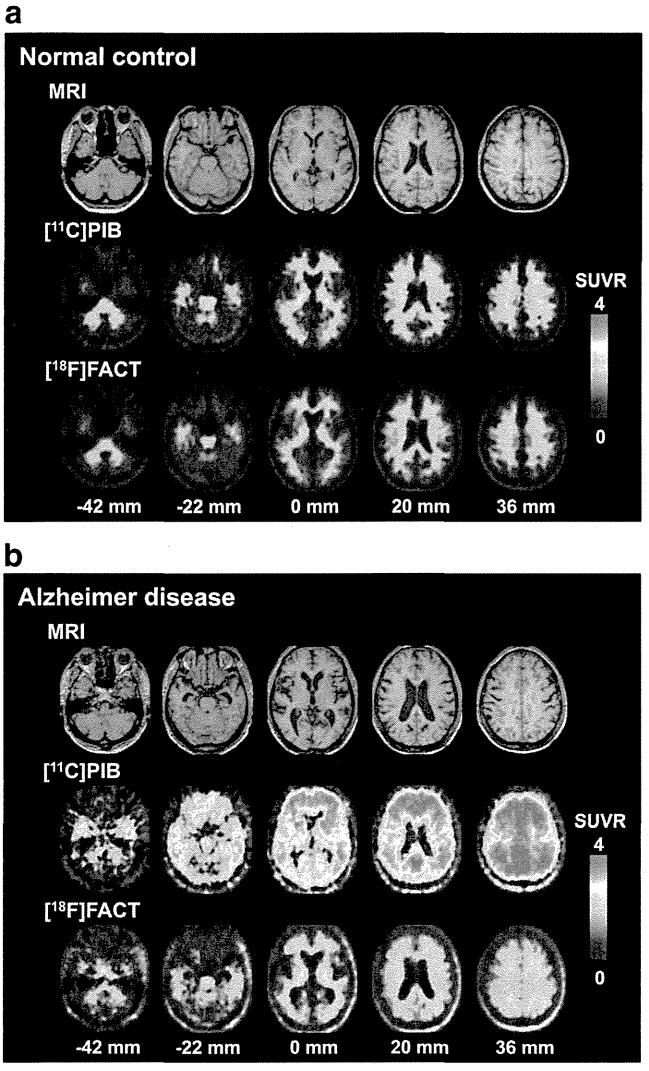

Fig. 1 Typical SUVR images of [^{11}C]PIB and [^{18}F]FACT studies and corresponding MR images (T1-weighted images) for a normal control subject (**a**) and an AD patient (**b**). Scale maximum and minimum values are 4 and 0 of SUVR. All images are transaxial sections parallel to the anterior-posterior commissure (AC-PC) line. Slice positions are −42, −22, 0, 20, and 36 mm from the AC-PC line. Anterior is at the top of the image and the subjects' right is on the left

Table 2 Average SUVR values of [^{11}C]PIB and [^{18}F]FACT studies

Region	[^{11}C]PIB	[^{18}F]FACT
Normal control subjects		
Frontal cortex	1.30±0.13	1.23±0.16
Temporal cortex	1.41±0.11	1.34±0.07
Parietal cortex	1.38±0.11	1.27±0.12
Occipital cortex	1.34±0.17	1.31±0.13
Parahippocampal gyrus	1.46±0.18	1.36±0.10
Posterior cingulate	1.64±0.15	1.49±0.08
Centrum semiovale	2.38±0.31	2.00±0.20
AD patients		
Frontal cortex	2.38±0.61**	1.14±0.13
Temporal cortex	2.14±0.37*	1.27±0.14
Parietal cortex	2.40±0.47*	1.29±0.11
Occipital cortex	1.84±0.27**	1.32±0.12
Parahippocampal gyrus	1.78±0.19***	1.31±0.07
Posterior cingulate	3.03±0.62*	1.61±0.18
Centrum semiovale	2.52±0.33	2.04±0.16

Values are shown as mean ± SD

Significant differences from normal control subjects (unpaired *t* test): **p* <0.001; ***p* <0.01; ****p* <0.05

Table 3 Average SUVR values in gray matter ($SUVR_{gray}$) of [^{11}C]PIB and [^{18}F]FACT studies

Region	[^{11}C]PIB	[^{18}F]FACT
Normal control subjects		
Frontal cortex	1.35±0.23	1.30±0.12
Temporal cortex	1.40±0.12	1.33±0.14
Parietal cortex	1.40±0.18	1.30±0.16
Occipital cortex	1.15±0.13	1.22±0.14
Parahippocampal gyrus	1.31±0.20	1.20±0.17
Posterior cingulate	1.60±0.25	1.44±0.18
AD patients		
Frontal cortex	4.91±1.63*	1.61±0.39****
Temporal cortex	3.53±0.98*	1.58±0.28****
Parietal cortex	4.57±1.47*	1.59±0.30****
Occipital cortex	3.10±1.28**	1.70±0.47***
Parahippocampal gyrus	2.72±0.58*	1.67±0.44***
Posterior cingulate	5.30±1.40*	2.02±0.43***

Values are shown as mean ± SD

Significant differences from normal control subjects (unpaired *t* test): **p* <0.001; ***p* <0.01; ****p* <0.05; *****p* <0.1

Autoradiographic and histochemical assays of postmortem brain slices

Formalin-fixed, paraffin-embedded sections were generated from brains of patients with definite AD (generously provided by Dr. Trojanowski and Dr. Lee, University of Pennsylvania). Six-μm-thick slices were incubated in 50 mM Tris-HCl buffer (pH 7.4) containing 5 % ethanol and [^{11}C]PIB (250 MBq/l, approximately 5 nM) at room temperature for 60 min. Nonspecific binding was determined in the presence of 10 μM of nonradioactive PIB. Following the reaction, the samples were rinsed with ice-cold Tris-HCl buffer twice for 2 min and dipped into ice-cold water for 10 s. The slices were subsequently dried under warm blowing air and contacted to an imaging plate (Fujifilm, Tokyo, Japan) for 2 h. The imaging plate data were scanned with a BAS-5000 system (Fujifilm). The intensity of radioactive signals was measured by MultiGauge® software (Fujifilm). These sections were then

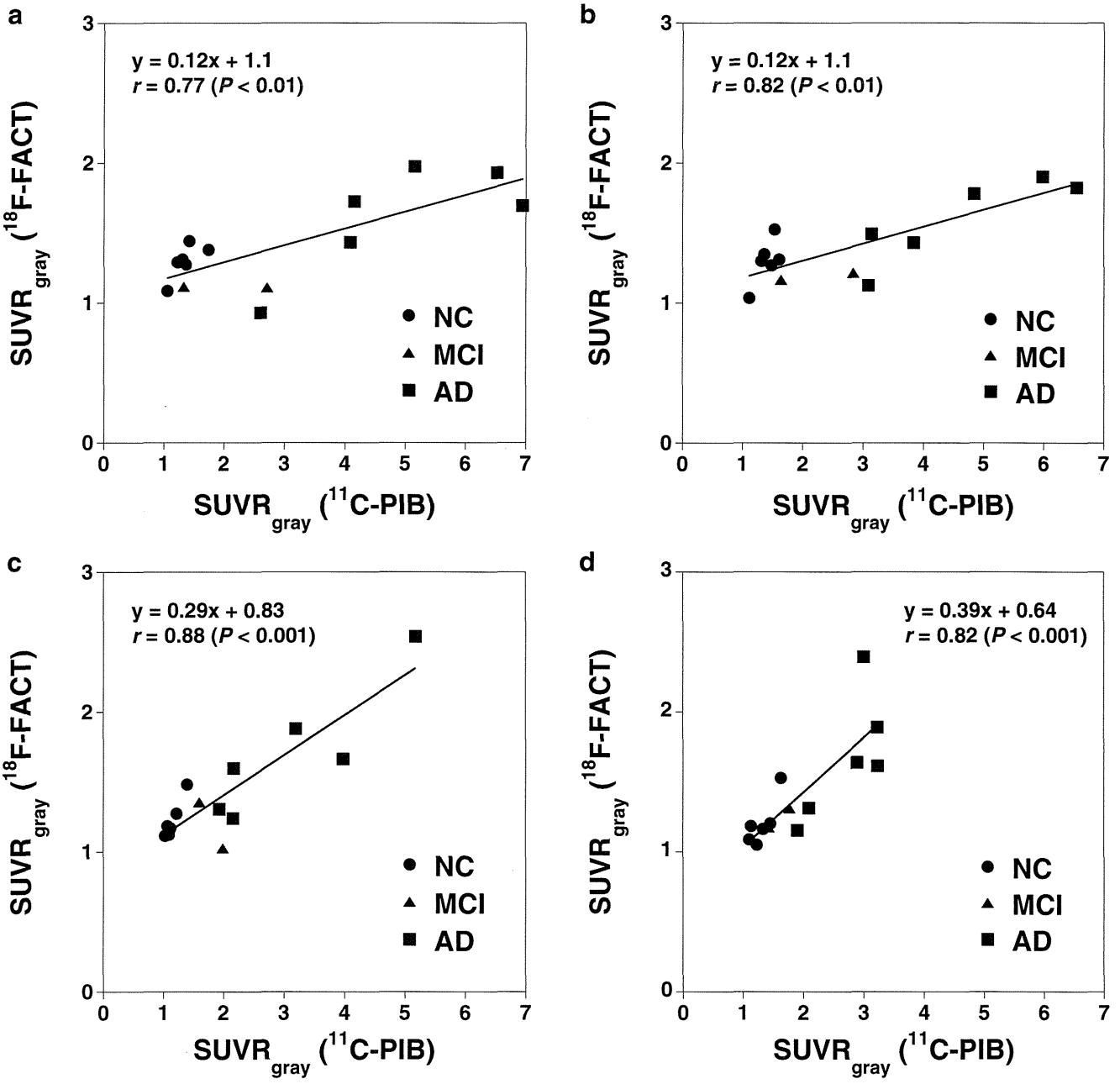

Fig. 2 The relationships of SUVR values in gray matter ($SUVR_{gray}$) between [^{11}C]PIB and [^{18}F]FACT studies for all subjects including normal control subjects (*NC*), mild cognitive impairment patients (*MCI*), and Alzheimer's disease patients (*AD*) in the frontal (**a**), parietal (**b**), occipital cortices (**c**), and parahippocampal gyrus (**d**)

labeled with [^{18}F]FACT 2 weeks after [^{11}C]PIB autoradiography. Briefly, the samples were reacted with [^{18}F]FACT (1 GBq/l, approximately 10 nM) dissolved in a reaction buffer identical to that used for [^{11}C]PIB at room temperature for 60 min. Nonspecific binding was determined in the presence of 10 μM of nonradioactive FACT. Tissue sections were then processed as in [^{11}C]PIB autoradiography and were contacted to an imaging plate for 15 min.

After radioactivity was allowed to decay, brain sections used for the autographic assay were fixed with 4 % paraformaldehyde in phosphate-buffered saline and were stained with 0.01 % (E,E)-1-fluoro-2,5-bis(3-hydroxycarbonyl-4-hydroxy)styrylbenzene (FSB, Dojindo Laboratories, Kumamoto, Japan), a fluorescent amyloid-binding compound, as described elsewhere [31]. Microscopic imaging was performed with an all-in-one microscope/digital camera (BZ-9000, Keyence, Osaka, Japan).

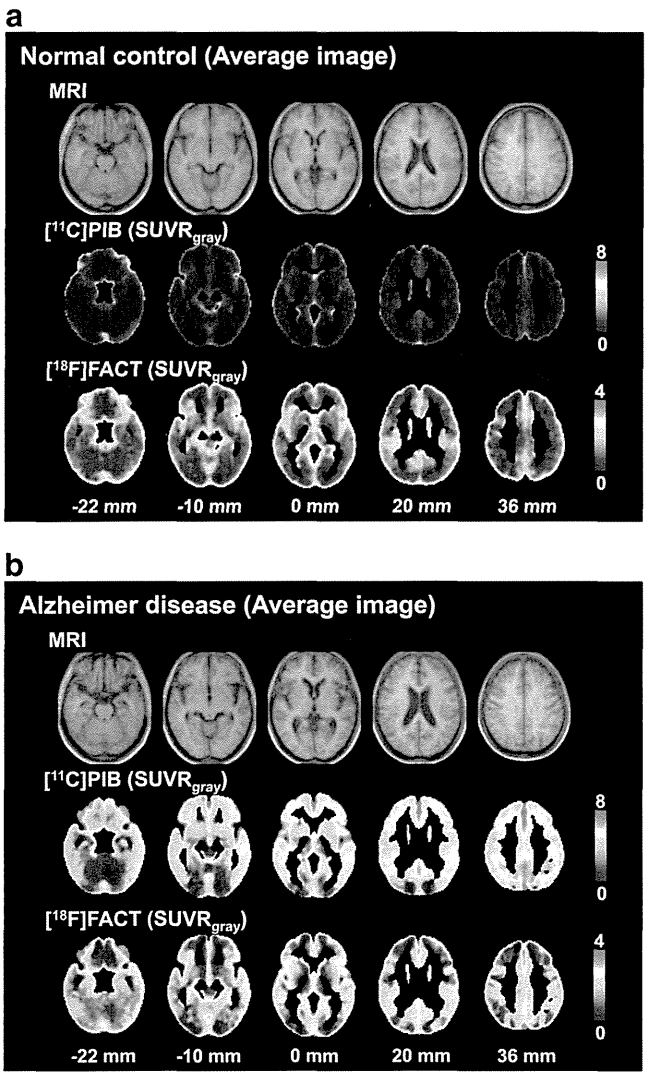

Fig. 3 Average images of SUVR in gray matter ($SUVR_{gray}$) of [^{11}C]PIB and [^{18}F]FACT studies and corresponding average MR images (T1-weighted images) for normal control subjects (**a**) and AD patients (**b**). Scale maximum and minimum values are 8 and 0 of $SUVR_{gray}$ for [^{11}C]PIB and 4 and 0 for [^{18}F]FACT studies. All images are transaxial sections parallel to the anterior-posterior commissure (AC-PC) line. Slice positions are −22, −10, 0, 20, and 36 mm from the AC-PC line. Anterior is at the top of the image and the subjects' right is on the left

Results

Typical SUVR images of [^{11}C]PIB and [^{18}F]FACT studies for a normal control subject are shown in Fig. 1a. Nonspecific accumulation in white matter was observed for both [^{11}C]PIB and [^{18}F]FACT. Typical SUVR images of [^{11}C]PIB and [^{18}F]FACT studies from an AD patient are shown in Fig. 1b. In AD patients, the cortical uptake indicating amyloid deposition was observed for both [^{11}C]PIB and [^{18}F]FACT. In the visual assessment of SUVR images, all normal control subjects and one of the MCI patients were diagnosed as negative for specific accumulation of [^{11}C]PIB, while all AD patients and the other MCI patient were diagnosed as positive.

The SUVR values of [^{11}C]PIB and [^{18}F]FACT studies in normal control subjects and AD patients are shown in Table 2. In [^{11}C]PIB studies, the SUVR values in all cerebral cortical regions were significantly larger in AD patients than in normal control subjects. However, in [^{18}F]FACT studies, no significant differences were observed between normal control subjects and AD patients in any of the brain regions.

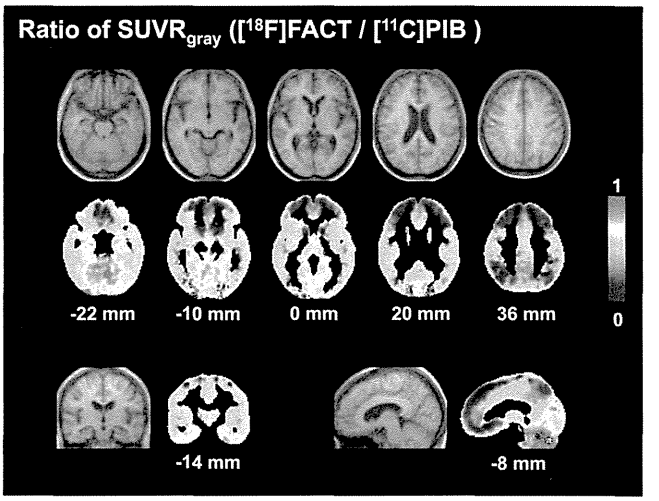

Fig. 4 Average images of ratio of SUVR in gray matter ($SUVR_{gray}$) of [^{18}F]FACT to [^{11}C]PIB studies for AD patients and corresponding average MR images (T1-weighted images). Scale maximum and minimum values are 1 and 0 of ratio. All transaxial images are parallel to the anterior-posterior commissure (AC-PC) line. Slice positions are −22, −10, 0, 20, and 36 mm from the AC-PC line. Anterior is at the top of the image and the subjects' right is on the left. The coronal image is perpendicular to the AC-PC line and its slice position is −14 mm (posterior side) from the AC. The subjects' right is on the left of the image. The sagittal image is parallel to the AC-PC line and its slice position is −8 mm (left side) from the AC-PC line. Anterior is on the left of the image

The $SUVR_{gray}$ values of [^{11}C]PIB and [^{18}F]FACT studies in normal control subjects and AD patients are shown in Table 3. In [^{11}C]PIB studies, the $SUVR_{gray}$ values in all cerebral cortical regions were significantly larger in AD patients than in normal control subjects. In [^{18}F]FACT studies, the $SUVR_{gray}$ value in the occipital cortex, parahippocampal gyrus, and posterior cingulate was significantly larger in AD patients than in normal control subjects. Trends of larger $SUVR_{gray}$ values in AD patients than in normal control subjects were observed in the frontal, temporal, and parietal cortices in the [^{18}F]FACT studies.

The relationships of $SUVR_{gray}$ values between [^{11}C]PIB and [^{18}F]FACT studies for all subjects are shown in Fig. 2. Significant positive correlations were observed in all brain regions. The slopes of linear regression lines (X: [^{11}C]PIB, Y: [^{18}F]FACT) ranged from 0.12 to 0.39. The greatest slopes were observed in the parahippocampal gyrus and occipital cortex, indicating relatively lower $SUVR_{gray}$ of [^{11}C]PIB and relatively higher $SUVR_{gray}$ of [^{18}F]FACT in these regions.

Average images of $SUVR_{gray}$ of [^{11}C]PIB and [^{18}F]FACT studies for normal control subjects and AD patients are shown in Fig. 3. Average images of the ratio of $SUVR_{gray}$ of [^{18}F]FACT to [^{11}C]PIB studies for AD patients are shown in Fig. 4. Relatively lower $SUVR_{gray}$ values of [^{11}C]PIB in distribution were observed in the medial side of the temporal cortex including the parahippocampal gyrus and occipital cortex as compared with [^{18}F]FACT. Relatively higher $SUVR_{gray}$ values of [^{11}C]PIB in distribution were observed in the frontal and parietal cortices.

The relationships between MMSE scores and $SUVR_{gray}$ of [^{11}C]PIB or [^{18}F]FACT studies for all AD patients and the one MCI patient positive for specific accumulation of [^{11}C]PIB are shown in Fig. 5. Significant positive correlations were observed in the temporal cortex for [^{11}C]PIB and in the frontal, parietal, and occipital cortices for [^{18}F]FACT. No significant correlation was observed in the parahippocampal gyrus and posterior cingulate for both [^{11}C]PIB and [^{18}F]FACT.

We then sought to identify pathological aggregates providing major binding components for [^{11}C]PIB and [^{18}F]FACT by comparative autoradiographic and histochemical assays of postmortem AD brain sections. Double autoradiographic labeling demonstrated distinct distribution of binding sites for these two radiotracers (Fig. 6a–c). Radio signals for [^{18}F]FACT were primarily observed in the hippocampal CA1 sector and subiculum besides white matter, in contrast to those for [^{11}C]PIB, which were most intense in the neocortex followed by the parahippocampal gyrus. No noticeable radiolabeling of [^{11}C]PIB and [^{18}F]FACT was detected in the hippocampal CA2 sector harboring numerous NFTs but few plaques (Fig. 6d), while [^{18}F]FACT signals in the CA1 and subiculum appeared to be associated with classic (dense-cored/neuritic) and compact plaques heavily deposited in these areas (Fig. 6e). Diffuse plaques, which were weakly labeled with FSB but involved no overt dystrophic changes of neurites, coexisted with NFTs in the parahippocampal gyrus (Fig. 6f) and therefore could be a source of moderate signals for [^{11}C]PIB. The fusiform gyrus was dominated by coreless

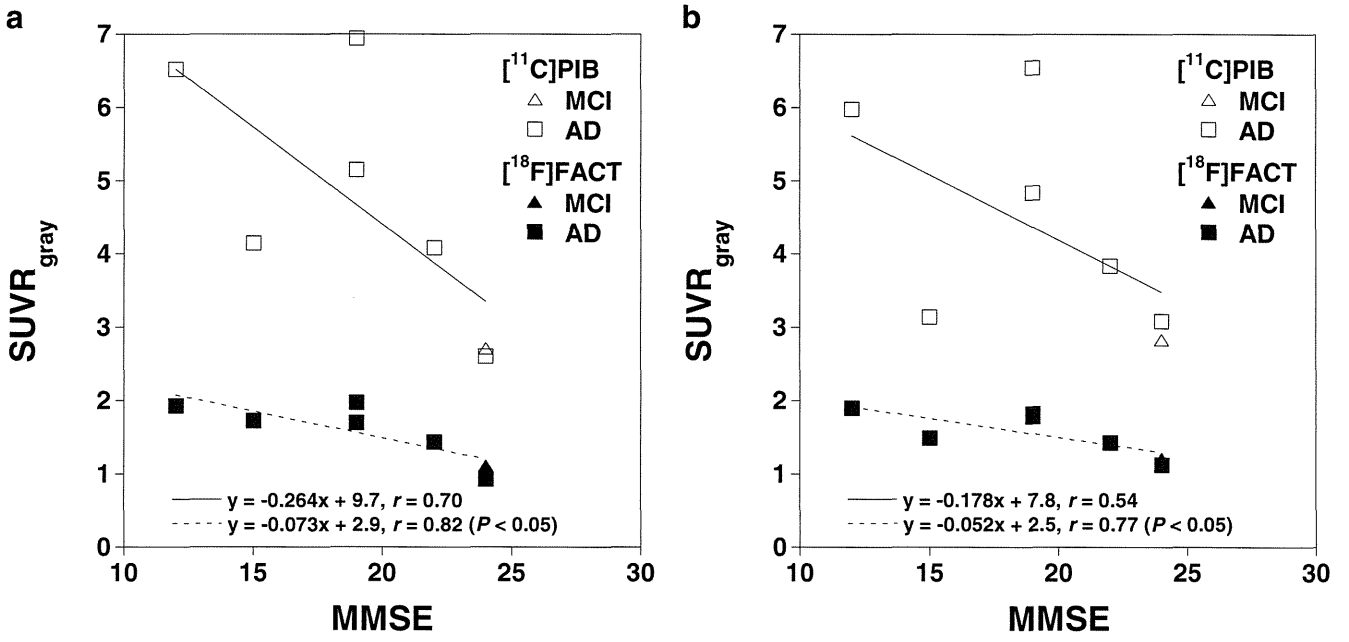

Fig. 5 The relationships between MMSE scores and SUVR values in gray matter (*$SUVR_{gray}$*) of [^{11}C]PIB or [^{18}F]FACT studies for all Alzheimer's disease patients (*AD*) and one patient with mild cognitive impairment (*MCI*) positive for specific accumulation of [^{11}C]PIB in the frontal (**a**) and parietal cortices (**b**)

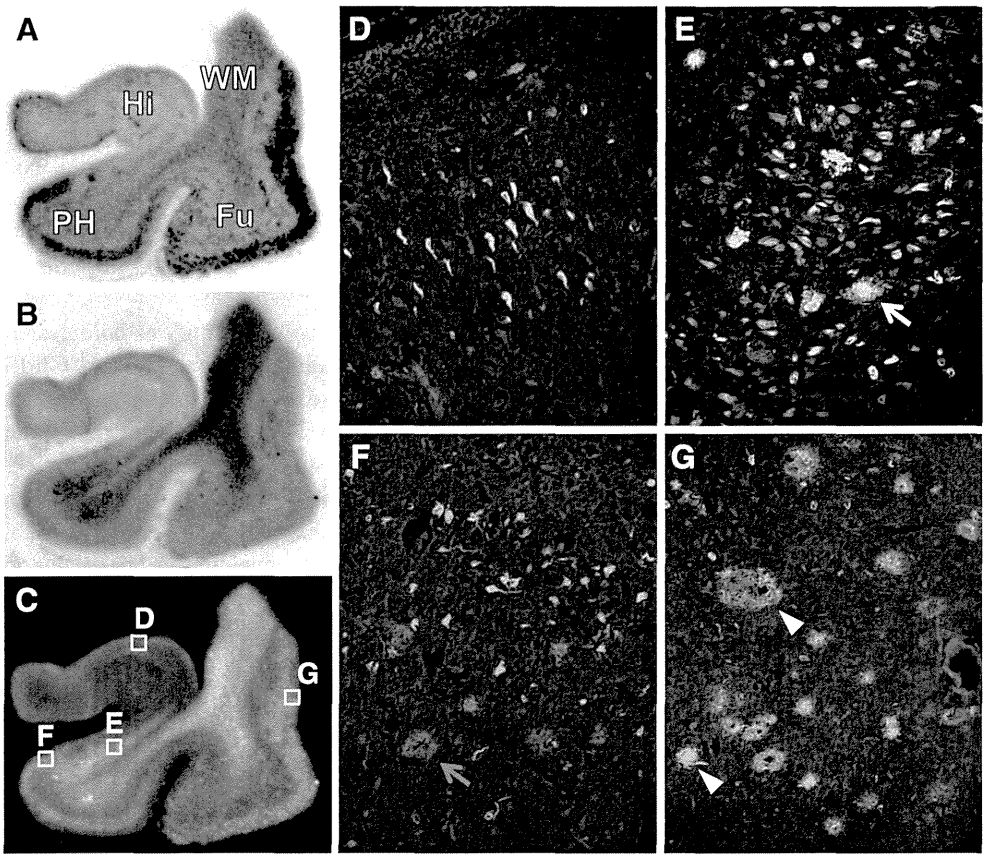

Fig. 6 Binding of [^{11}C]PIB and [^{18}F]FACT to distinct subtypes of senile plaques in AD patient brains. **a**, **b** Autoradiographic labeling of a single AD brain slice with [^{11}C]PIB (**a**) and [^{18}F]FACT (**b**). The section contains the hippocampus (*Hi*), parahippocampal gyrus (*PH*), fusiform gyrus (*Fu*), and white matter (*WM*). **c** Superimposition of autoradiograms displayed in **a** and **b**. *Red* and *green* signals indicate binding of [^{11}C]PIB and [^{18}F]FACT, respectively. *Squares* represent subregions from which photomicrographs shown in **d**–**g** were acquired. **d**–**g** Histofluorescence staining of amyloid lesions with FSB in the section used for autoradiography. NFTs with few plaques were observed in the hippocampal CA2 region (**d**), while classic and compact plaques (*white arrow*) with dense cores coexisted with NFTs in the subiculum (**e**). In the parahippocampal gyrus (**f**), NFTs were abundant in concurrence with diffuse plaques faintly illuminated with FSB (*red arrow*). The fusiform gyrus (**g**) was dominated by primitive plaques containing dystrophic neurites (*arrowheads*)

primitive plaques with FSB-positive neurites (Fig. 6g), accounting for the strong reactivity of [^{11}C]PIB with this region.

Discussion

While the SUVR values of [^{11}C]PIB were significantly larger in AD patients than in normal control subjects, no significant differences were observed between normal control subjects and AD patients in [^{18}F]FACT studies. In both [^{11}C]PIB and [^{18}F]FACT studies, nonspecific accumulation in white matter was observed, and this must hamper the quantitative analysis of cortical uptake of radiotracer due to the limited spatial resolution of the PET scanner. To remove the effects of white matter accumulation, $SUVR_{gray}$ values were calculated using gray and white matter images extracted from MR images according to the method developed by Müller-Gärtner et al. [29]. This partial volume correction technique was also originally used for estimation of cerebral blood flow per gray matter fraction in an ROI [30]. The $SUVR_{gray}$ values were larger in AD patients than in normal control subjects in both [^{11}C]PIB and [^{18}F]FACT studies. Since several radiotracers for amyloid imaging show the nonspecific accumulation in white matter [4, 7, 8, 18], such partial volume correction will be needed to estimate the deposition of amyloid senile plaques in cerebral cortices by PET. On the other hand, a recently developed radiotracer for amyloid deposits [^{11}C]AZD2184 which shows no conspicuous accumulation in white matter may not need such partial volume correction [10].

Although the $SUVR_{gray}$ values of [^{18}F]FACT were smaller than those of [^{11}C]PIB in AD patients, good correlations were observed in $SUVR_{gray}$ values between [^{11}C]PIB and [^{18}F]FACT studies, indicating the validity of [^{18}F]FACT as a radiotracer for amyloid imaging. Comparing $SUVR_{gray}$ images between [^{11}C]PIB and [^{18}F]FACT, relatively lower $SUVR_{gray}$ values of [^{11}C]PIB in distribution were observed in the parahippocampal gyrus and occipital cortex as compared with [^{18}F]FACT. Relatively higher $SUVR_{gray}$ values of

[^{11}C]PIB in distribution were also observed in the frontal and parietal cortices. A radiotracer for amyloid imaging, [^{11}C]BF227, has been considered to bind more preferentially to dense-cored amyloid deposition than [^{11}C]PIB [7]. [^{18}F]FACT has a structure similar to [^{11}C]BF227 and therefore it also binds more preferentially to dense-cored amyloid deposition [18]. If the cerebral cortical uptake of [^{11}C]PIB might be due to binding to both diffuse and dense-cored amyloid plaque [32], such regional differences in cerebral cortical uptake between [^{11}C]PIB and [^{18}F]FACT might be due to differences in regional distribution between diffuse and dense-cored amyloid plaque. In the present study, the autoradiographic and histochemical assays of postmortem AD brain sections also showed that [^{18}F]FACT signals were associated with classic (dense-cored/neuritic) and compact plaques, and diffuse plaques could be a source of moderate signals for [^{11}C]PIB. A histopathological study showed that diffuse amyloid plaques were not prominent in the occipital lobe as compared with the frontal and temporal lobes [33]. This might correspond to the relatively lower $SUVR_{gray}$ of [^{11}C]PIB in the occipital cortex as compared to that of [^{18}F]FACT observed in the present study.

It has been reported that synapse loss was accentuated within immature and mature plaques, but not within diffuse plaques [16]. Since [^{18}F]FACT might bind more preferentially to dense-cored amyloid plaques, [^{18}F]FACT binding might be an indicator of the severity of AD. In the present study, significant positive correlations were observed between MMSE scores and $SUVR_{gray}$ of [^{18}F]FACT in many of the neocortical regions, but not in [^{11}C]PIB as also shown in previous studies [34]. Although the number of the subjects is rather small to investigate the correlation between MMSE scores and $SUVR_{gray}$, this indicates that cortical accumulation of [^{18}F]FACT can reflect the severity of AD to a greater extent than [^{11}C]PIB.

In conclusion, deposition of amyloid senile plaques was measured by PET with both [^{11}C]PIB and [^{18}F]FACT in the same subjects, including normal control subjects, MCI patients, and AD patients. After partial volume correction to remove the effects of white matter accumulation, cerebral cortical uptake was larger in AD patients than in normal control subjects in both [^{11}C]PIB and [^{18}F]FACT studies. Regional differences in cerebral cortical uptake were observed between [^{11}C]PIB and [^{18}F]FACT, possibly due to differences in regional distribution between diffuse and dense-cored amyloid plaques.

Acknowledgments This study was supported in part by "Japan Advanced Molecular Imaging Program (J-AMP)" of the Ministry of Education, Culture, Sports, Science and Technology (MEXT), Japanese Government, a Grant-in-Aid for Comprehensive Research on Dementia (No. 11103404) from the Ministry of Health, Labour and Welfare, and a Grant-in-Aid from the Mitsubishi Pharma Research Foundation. We thank Mr. Katsuyuki Tanimoto and Mr. Takahiro Shiraishi for their assistance in performing the PET experiments at the National Institute of Radiological Sciences. We also thank Ms. Kazuko Suzuki and Ms. Izumi Izumida of the National Institute of Radiological Sciences for their help as clinical research coordinators.

Conflicts of interest None.

References

1. Braak H, Braak E. Neuropathological stageing of Alzheimer-related changes. Acta Neuropathol 1991;82:239–59.
2. Hardy JA, Higgins GA. Alzheimer's disease: the amyloid cascade hypothesis. Science 1992;256:184–5.
3. Mathis CA, Wang Y, Holt DP, Huang GF, Debnath ML, Klunk WE. Synthesis and evaluation of 11C-labeled 6-substituted 2-arylbenzothiazoles as amyloid imaging agents. J Med Chem 2003;46:2740–54.
4. Klunk WE, Engler H, Nordberg A, Wang Y, Blomqvist G, Holt DP, et al. Imaging brain amyloid in Alzheimer's disease with Pittsburgh Compound-B. Ann Neurol 2004;55:306–19.
5. Agdeppa ED, Kepe V, Liu J, Flores-Torres S, Satyamurthy N, Petric A, et al. Binding characteristics of radiofluorinated 6-dialkylamino-2-naphthylethylidene derivatives as positron emission tomography imaging probes for beta-amyloid plaques in Alzheimer's disease. J Neurosci 2001;21:RC189.
6. Ono M, Wilson A, Nobrega J, Westaway D, Verhoeff P, Zhuang ZP, et al. 11C-labeled stilbene derivatives as Abeta-aggregate-specific PET imaging agents for Alzheimer's disease. Nucl Med Biol 2003;30:565–71.
7. Kudo Y, Okamura N, Furumoto S, Tashiro M, Furukawa K, Maruyama M, et al. 2-(2-[2-Dimethylaminothiazol-5-yl]ethenyl)-6-(2-[fluoro]ethoxy)benzoxazole: a novel PET agent for in vivo detection of dense amyloid plaques in Alzheimer's disease patients. J Nucl Med 2007;48:553–61.
8. Rowe CC, Ackerman U, Browne W, Mulligan R, Pike KL, O'Keefe G, et al. Imaging of amyloid beta in Alzheimer's disease with 18F-BAY94-9172, a novel PET tracer: proof of mechanism. Lancet Neurol 2008;7:129–35.
9. Choi SR, Golding G, Zhuang Z, Zhang W, Lim N, Hefti F, et al. Preclinical properties of 18F-AV-45: a PET agent for Aβ plaques in the brain. J Nucl Med 2009;50:1887–94.
10. Nyberg S, Jönhagen ME, Cselényi Z, Halldin C, Julin P, Olsson H, et al. Detection of amyloid in Alzheimer's disease with positron emission tomography using [11C]AZD2184. Eur J Nucl Med Mol Imaging 2009;36:1859–63.
11. Cselényi Z, Jönhagen ME, Forsberg A, Halldin C, Julin P, Schou M, et al. Clinical validation of 18F-AZD4694, an amyloid-beta-specific PET radioligand. J Nucl Med 2012;53:415–24.
12. Buckner RL, Snyder AZ, Shannon BJ, LaRossa G, Sachs R, Fotenos AF, et al. Molecular, structural, and functional characterization of Alzheimer's disease: evidence for a relationship between default activity, amyloid, and memory. J Neurosci 2005;25:7709–17.
13. Engler H, Forsberg A, Almkvist O, Blomquist G, Larsson E, Savitcheva I, et al. Two-year follow-up of amyloid deposition in patients with Alzheimer's disease. Brain 2006;129:2856–66.
14. Rowe CC, Ng S, Ackermann U, Gong SJ, Pike K, Savage G, et al. Imaging β-amyloid burden in aging and dementia. Neurology 2007;68:1718–25.
15. Wang J, Dickson DW, Trojanowski JQ, Lee VM. The levels of soluble versus insoluble brain Aβ distinguish Alzheimer's disease from normal and pathologic aging. Exp Neurol 1999;158:328–37.

16. Masliah E, Terry RD, Mallory M, Alford M, Hansen LA. Diffuse plaques do not accentuate synapse loss in Alzheimer's disease. Am J Pathol 1990;137:1293–7.
17. Price JL. Diagnostic criteria for Alzheimer's disease. Neurobiol Aging 1997;18:S67–70.
18. Furumoto S, Okamura N, Furukawa K, Tashiro M, Ishikawa Y, Sugi K, et al. A 18F-labeled BF-227 derivative as a potential radioligand for imaging dense amyloid plaques by positron emission tomography. Mol Imaging Biol 2013;15:497–506.
19. Shidahara M, Tashiro M, Okamura N, Furumoto S, Furukawa K, Watanuki S, et al. Evaluation of the biodistribution and radiation dosimetry of the 18F-labelled amyloid imaging probe [18F]FACT in humans. EJNMMI Res 2013;3:32.
20. McKhann G, Drachman D, Folstein M, Katzman R, Price D, Stadlan EM. Clinical diagnosis of Alzheimer's disease: report of the NINCDS-ADRDA Work Group under the auspices of Department of Health and Human Services Task Force on Alzheimer's Disease. Neurology 1984;34:939–44.
21. Morris JC. The Clinical Dementia Rating (CDR): current version and scoring rules. Neurology 1993;43:2412–4.
22. Folstein MF, Folstein SE, McHugh PR. "Mini-mental state". A practical method for grading the cognitive state of patients for the clinician. J Psychiatr Res 1975;12:189–98.
23. Matsumoto K, Kitamura K, Mizuta T, Tanaka K, Yamamoto S, Sakamoto S, et al. Performance characteristics of a new 3-dimensional continuous-emission and spiral-transmission high-sensitivity and high-resolution PET camera evaluated with the NEMA NU 2-2001 standard. J Nucl Med 2006;47:83–90.
24. Ishikawa A, Kitamura K, Mizuta T, Tanaka K, Amano M, Inoue Y, et al. Implementation of on-the-fly scatter correction using dual energy window method in continuous 3D whole body PET scanning. IEEE Nucl Sci Symp Conf Rec 2005;5:2497–500.
25. Price JC, Klunk WE, Lopresti BJ, Lu X, Hoge JA, Ziolko SK, et al. Kinetic modeling of amyloid binding in humans using PET imaging and Pittsburgh Compound-B. J Cereb Blood Flow Metab 2005;25:1528–47.
26. Ito H, Hietala J, Blomqvist G, Halldin C, Farde L. Comparison of the transient equilibrium and continuous infusion method for quantitative PET analysis of [11C]raclopride binding. J Cereb Blood Flow Metab 1998;18:941–50.
27. Friston KJ, Frith CD, Liddle PF, Dolan RJ, Lammertsma AA, Frackowiak RS. The relationship between global and local changes in PET scans. J Cereb Blood Flow Metab 1990;10:458–66.
28. Ashburner J, Friston KJ. Voxel-based morphometry–the methods. Neuroimage 2000;11:805–21.
29. Müller-Gärtner HW, Links JM, Prince JL, Bryan RN, McVeigh E, Leal JP, et al. Measurement of radiotracer concentration in brain gray matter using positron emission tomography: MRI-based correction for partial volume effects. J Cereb Blood Flow Metab 1992;12:571–83.
30. Ito H, Inoue K, Goto R, Kinomura S, Taki Y, Okada K, et al. Database of normal human cerebral blood flow measured by SPECT: I. Comparison between I-123-IMP, Tc-99m-HMPAO, and Tc-99m-ECD as referred with O-15 labeled water PET and voxel-based morphometry. Ann Nucl Med 2006;20:131–8.
31. Higuchi M, Iwata N, Matsuba Y, Sato K, Sasamoto K, Saido TC. 19F and 1H MRI detection of amyloid beta plaques in vivo. Nat Neurosci 2005;8:527–33.
32. Ikonomovic MD, Klunk WE, Abrahamson EE, Mathis CA, Price JC, Tsopelas ND, et al. Post-mortem correlates of in vivo PiB-PET amyloid imaging in a typical case of Alzheimer's disease. Brain 2008;131:1630–45.
33. Yamaguchi H, Hirai S, Morimatsu M, Shoji M, Harigaya Y. Diffuse type of senile plaques in the brains of Alzheimer-type dementia. Acta Neuropathol 1988;77:113–9.
34. Jack Jr CR, Lowe VJ, Senjem ML, Weigand SD, Kemp BJ, Shiung MM, et al. 11C PiB and structural MRI provide complementary information in imaging of Alzheimer's disease and amnestic mild cognitive impairment. Brain 2008;131:665–80.

Neuroscience Letters 581 (2014) 103–108

Contents lists available at ScienceDirect

Neuroscience Letters

journal homepage: www.elsevier.com/locate/neulet

Biological evaluation of the radioiodinated imidazo[1,2-*a*]pyridine derivative DRK092 for amyloid-β imaging in mouse model of Alzheimer's disease

Chun-Jen Chen[a,b,c], Kazunori Bando[a], Hiroki Ashino[a], Kazumi Taguchi[a], Hideaki Shiraishi[a], Keiji Shima[a], Osuke Fujimoto[a], Chiemi Kitamura[a], Yasuaki Morimoto[a], Hiroyuki Kasahara[a], Takao Minamizawa[a], Cheng Jiang[d], Ming-Rong Zhang[b], Tetsuya Suhara[b], Makoto Higuchi[b], Kazutaka Yamada[c,**], Bin Ji[b,*]

[a] *Research Department, Fujifilm RI Pharma Co. LTD., Chiba, Japan*
[b] *Molecular Imaging Center, National Institute of Radiological Sciences, Chiba, Japan*
[c] *Clinical Veterinary Science, The United Graduate School of Veterinary Science, Gifu University, Gifu, Japan*
[d] *School of Pharmacy, Fudan University, Shanghai, China*

HIGHLIGHTS

- DRK092 has higher affinity for fibrillary Aβ and brain uptake than IMPY.
- ^{125}I-DRK092 labeled Aβ deposited in brains of AD patient and mouse in vitro.
- ^{125}I-DRK092 detected Aβ accumulation more sensitively than ^{125}I-IMPY ex vivo.

GRAPHICAL ABSTRACT

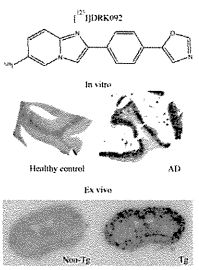

ARTICLE INFO

Article history:
Received 7 June 2014
Received in revised form 31 July 2014
Accepted 19 August 2014
Available online 27 August 2014

Keywords:
Alzheimer's disease (AD)
Amyloid-β peptide (Aβ)
Amyloid precursor protein (APP) transgenic mouse
DRK092
IMPY
Single photon emission computed tomography (SPECT)

ABSTRACT

Non-invasive determination of amyloid-β peptide (Aβ) deposition has important significance for early diagnosis and medical intervention in Alzheimer's disease (AD). In this study, we investigated the availability of a radioiodinated imidazo[1,2-*a*]pyridine derivative, termed ^{125}I-DRK092, as single photon emission computed tomography (SPECT) ligand for in vivo detection of Aβ deposition. DRK092 showed high binding affinity for either synthetic human Aβ fibrils or brain homogenates from amyloid precursor protein transgenic (Tg) mouse (PS1-ki/JU-Tg2576) and AD patient with a dissociation constant (K_d) of one-digit nM, and excellent brain permeability (peak value of uptake: approximately 0.9% of injection dose/g rat brain). Ex vivo autoradiographic analysis showed that measurement with ^{125}I-DRK092 has higher sensibility for detecting Aβ accumulation than with ^{125}I-IMPY, a well-known amyloid SPECT ligand, in Tg mice. In vitro autoradiography with ^{125}I-DRK092 also confirmed higher accumulation of radioactivity in the cortical area, enriched with Aβ plaques, of Tg mouse and AD patient brains, as compared with the corresponding areas in non-Tg mouse and healthy control brains. All the data presented above lead us to draw the conclusion that radioiodinated DRK092 is a potential SPECT ligand for amyloid imaging in AD.

* Corresponding author at: Molecular Imaging Center, National Institute of Radiological Sciences, 4-9-1, Anagawa, Inage-ku, Chiba, Chiba 263-8555, Japan. Tel.: +81 43 206 3251; fax: +81 43 253 0396.
** Corresponding author at: The United Graduate School of Veterinary Science, Gifu University, 1-1 Yanagido, Gifu City 501-1193, Japan. Tel.: +81 155 49 5395; fax: +81 155 49 5398.
E-mail addresses: kyamada@obihiro.ac.jp (K. Yamada), kihin@nirs.go.jp (B. Ji).

http://dx.doi.org/10.1016/j.neulet.2014.08.036
0304-3940/

1. Introduction

Alzheimer's disease (AD) is a progressive neurodegenerative disorder characterized by the two pathological hallmarks of amyloid-β peptide (Aβ) plaques and neurofibrillary tangles. In vivo non-invasive detection of Aβ deposition is important for early diagnosis and medical intervention of AD at prodromal stage, since fibrillary Aβ has already been accumulating in the brain for a few decades before onset of AD [1]. Over the past few years, the availabilities of several positron emission tomography (PET) tracers for amyloid imaging have successfully been verified in human patients with AD and model animals with amyloid pathology [2–5]. Although being inferior to PET in sensitivity and quantitative performance, single photon emission computed tomography (SPECT) imaging has advantages in terms of operating cost and already-installed rate in medical hospitals, and is thereby more suitable for primary screening for prodromal AD patients. To date, a number of iodinated ligands, such as diphenyl-1,3,4-oxadiazole (1,3,4-DPOD) derivatives [6], aurone derivatives [7], 1,4-diphenyltriazole derivatives [8], pyridyl benzofuran derivatives [9], and imidazo[1,2-***a***]pyridine derivatives [10] have been employed for amyloid imaging with SPECT. IMPY, an imidazo[1,2-***a***]pyridine derivative, is the only ligand for SPECT that has been tested in humans [11]. Although this ligand has shown excellent properties as an imaging probe in preclinical studies [12,13], the preliminary clinical data for ^{123}I-IMPY showed a poor signal-to-noise ratio, possibly making it difficult to distinguish between cognitively normal persons and AD patients [14]. Very recently, we synthesized a series of imidazo[1,2-***a***]pyridine derivatives with higher affinity for synthetic human Aβ fibrils for amyloid SPECT imaging. In the present study, we examined the potential of one promising candidate compound, termed DRK092, by performing in vitro and ex vivo autoradiographic analyses of a the model mouse with AD-like amyloid pathology and postmortem human tissues.

2. Materials and methods

2.1. Radiosynthesis of radioligands

Radiosynthesis of ^{125}I-DRK092 and ^{125}I-IMPY was performed as described in previous publications [10,15]. The radiochemical purity of ^{125}I-DRK092 and ^{125}I-IMPY was 99.5 ± 0.27% (mean ± SE; n = 3) and 99.6 ± 0.25% (n = 4), respectively, and specific radioactivity was 81.4 and 81.4 GBq/μmol, respectively, at the end of synthesis.

2.2. Experimental animals

We had obtained the JU-Tg2576 mouse, generated by backcross of a transgenic (Tg) mouse line (Tg2576; Taconic Farms Inc. New York, NY), which overexpressed a mutant form of amyloid precursor protein (APPK670/671L), with JU strain (JU/Ct-C, A.) mouse over 29 generations, under license agreement with the Mayo Foundation for Medical Education and Research (Rochester, MN), from Daiichi Sankyo Co. Ltd. (Tokyo, Japan) for easier daily handling. Furthermore, we crossbred the JU-Tg2576 mouse with a "knock-in" mouse with the I213T preseniline-1 (PS1) missense mutation (PS1-ki) [16] to generate PS1-ki/JU-Tg2576 mouse for earlier amyloid pathogenesis. Tg mice (indicated as PS1-ki/JU-Tg2576 if without special description) and body-weight matched non-Tg JU strain mice as control animals were used in the present study except for the in vitro autoradiographic experiment, in which commercially available Tg2576 mouse brain was used.

2.3. Preparation of brain homogenates and Aβ fibrils

The Tg mice were deeply anesthetized and euthanized by decapitation. The neocortex was rapidly removed and homogenized with Potter-Elvehjem homogenizer (Thermo Fisher Scientific Inc., Philadelphia, PA) in 5 volumes of 20 mM Tris–HCl buffer (pH 7.6) containing protease inhibitor cocktail (Nacalai Tesque Inc., Kyoto, Japan) and 0.25 M sucrose. Aliquots of the homogenates were immediately frozen and stored at −80 degree until the experiments. The homogenates of gray matter from the parahippocampal gyrus from an 89-year-old patient with AD (Harvard Brain Tissue Resource Center and Analytical Biological Services, Inc.) were prepared using the same method. Aβ fibrils were generated by spontaneous assembly. Briefly, lyophilized synthetic Aβ(1-40) peptides (Peptide Institute Inc. Osaka, Japan, final concentration: 100 μM) were gently dissolved in 10 mM phosphate buffered saline (PBS, pH7.4) containing 1 mM EDTA and incubated at 37 °C for 4 days with gentle, constant shaking. Aggregated Aβ fibrils were stored at 4 °C and diluted into working solution (final concentration: 0.5 μM) for in vitro binding assay.

2.4. In vitro binding assay

The 100-μl aliquots of Aβ fibrils working solutions or brain homogenates were reacted with 900 μl of PBS containing ascorbic acid (final concentration: 20 mM) and ^{125}I-DRK092 or ^{125}I-IMPY (20 kBq; final concentrations were adjusted to serial concentrations of 0.2–100 nM for synthetic Aβ fibril or 0.1–500 nM for brain homogenate incubation solutions by the addition of non-radiolabeled DRK092 or IMPY). The reaction mixtures were incubated at 37 °C for 1 h, followed by vacuum filtration through Whatman GF/B filters using a Brandel cell harvester (Model M-24R, Biomedical Research. Lab., Gaithesburg, MD). Radioactivity on the GF/B filters was measured by gamma counter after three rapid washes with 2 ml of ice-cold PBS containing 0.1 mM ascorbic acid. The dissociation constant (K_d) and maximum specific binding (B_{max}) were generated by Scatchard analysis using a GraphPad Prism (GraphPad Software, version 4.3, San Diego, CA, USA).

2.5. In vitro autoradiographic analysis

Fresh frozen brain sections (20-μm thickness) from a 23-month-old Tg2576 Tg mouse and deparaffinized human brain sections (10-μm thickness; Center for Neurodegenerative Disease Research at the University of Pennsylvania Perelman School of Medicine) were preincubated with PBS for 30 min, followed by incubation with ^{125}I-DRK092 (2 nM) in PBS containing 20% ethanol in the absence or presence of non-radiolabeled DRM106, an analog of DRK092 with high affinity for Aβ fibrils [15], at room temperature for 1 h. After that, the sections were rinsed with ice-cold PBS containing 20% ethanol 2 times for 2 min each time, and finally dipped into distilled water for 10 s. After warmly blow-dried and attached to an imaging plate (BAS-MS2025; Fujifilm, Tokyo, Japan) for 3 days, radiolabeling was detected by scanning the imaging plate using the BAS-5000 system (Fujifilm).

2.6. Ex vivo autoradiographic analysis

Male Tg mice (19 months old) and age-matched non-Tg littermate mice received bolus injection of radioligands (1.3 MBq of ^{125}I-DRK092 or ^{125}I-IMPY in 0.2 ml of saline containing 1% tween80 and 40 mM sodium L-ascorbate) via tail vein. At indicated time points, the animals were deeply anesthetized with isoflurane and euthanized by decapitation. The brains were immediately removed, embedded in Tissue-Tec. O.C.T. Compound (Sakura Finetechnical Co., Ltd., Tokyo, Japan), frozen in dry ice, and cut into 15-μm thick